AGU PUBLICATIONS

JGR

Journal of Geophysical Research: Solid Earth

RESEARCH ARTICLE

10.1002/2013JB010405

Key Points:
- The loci of maximum fluid pressure coincide with biggest sediment compaction
- High fluid pressure and a very weak decollement can explain the wedge geometry
- Permeable faults and mud volcano conduits are important fluid pathways

Correspondence to:
S.-K. Kufner,
kufner@gfz-potsdam.de

Citation:
Kufner, S.-K., A. Hüpers, and A. J. Kopf (2014), Constraints on fluid flow processes in the Hellenic Accretionary Complex (eastern Mediterranean Sea) from numerical modeling, *J. Geophys. Res. Solid Earth*, *119*, 3601–3626, doi:10.1002/2013JB010405.

Received 31 MAY 2013
Accepted 9 MAR 2014
Accepted article online 16 MAR 2014
Published online 10 APR 2014

Constraints on fluid flow processes in the Hellenic Accretionary Complex (eastern Mediterranean Sea) from numerical modeling

S.-K. Kufner[1,2,3], A. Hüpers[1], and A. J. Kopf[1]

[1]Marine Geotechnics, Center of Environmental Sciences, University of Bremen, Bremen, Germany, [2]Geophysical Institute, Karlsruhe Institute of Technology, Karlsruhe, Germany, [3]Lithosphere Dynamics, German Research Center for Geosciences, Potsdam, Germany

Abstract The dynamics of accretionary convergent margins are severely influenced by intense deformation and fluid expulsion. To quantify the fluid pressure and fluid flow velocities in the Hellenic subduction system, we set up 2-D hydrogeological numerical models following two seismic reflection lines across the Mediterranean Ridge. These profiles bracket the along-strike variation in wedge geometry: moderate compression and a >4 km thick underthrust sequence in the west versus enhanced compression and <1 km of downgoing sediment in the center. Input parameters were obtained from preexisting geophysical data, drill cores, and new geotechnical laboratory experiments. A permeability-porosity relationship was determined by a sensitivity analysis, indicating that porosity and intrinsic permeability are small. This hampers the expulsion of fluids and leads to the build up of fluid overpressure in the deeper portion of the wedge and in the underthrust sediment. The loci of maximum fluid pressure are mainly controlled by the compactional fluid source, which generally decreases toward the backstop. However, pore pressure is still high at the decollement level at distances <100 km from the deformation front, either by the incorporation of low permeability evaporites or additional compaction of the wedge sediments in the two profiles. In the west, however, formation of a wide accretionary complex is facilitated by high pore pressure zones. When compared to other large accretionary complexes such as Nankai or Barbados, our results not only show broad similarities but also that near-lithostatic pore pressures may be easier to maintain in the Hellenic Arc because of accentuated collision, some underthrust evaporates, and a thicker underthrust sequence.

1. Introduction

At approximately 50% of the subduction zones worldwide the sediments overlying the incoming oceanic plate are partly accumulated in front of the leading edge of the overriding plate and form an accretionary prism [*Clift and Vannucchi*, 2004]. The width and the taper angle of accretionary prisms depend on various factors, including the total rate of plate convergence, the wedge outbuilding rate, the sediment supply, the sediment physical properties, and the involvement of fluids [*Saffer and Bekins*, 2006; *Clift and Vannucchi*, 2004]. From these factors influencing the general shape of an accretionary complex, fluids play a crucial role on the fore-arc mechanics of subduction zones and the occurrence of earthquakes [*Saffer and Bekins*, 2006; *Moore and Saffer*, 2001]. Fluid overpressures reduce the effective stress, which results in smaller shear strength and mediate the slip behavior of faults [*Saffer and Tobin*, 2011]. Fluid sources within the complex arise due to the release of intergranular pore water within the sediments and bound water from hydrous minerals. However, it is difficult to constrain the impact of fluids on a broader scale by in situ measurements. Here, numerical modeling becomes a useful tool to quantify the effects of fluids in accretionary complexes [*Saffer and Bekins*, 1998; *Bekins et al.*, 1995; *Bekins and Dreiss*, 1992; *Henry and Wang*, 1991; *Screaton et al.*, 1990; *Shi et al.*, 1989].

In the past, hydrogeological models focused on accretionary margins such as Nankai [*Saffer and Bekins*, 1998], Barbados [*Bekins et al.*, 1995], Peru [*Matmon and Bekins*, 2006], or Cascadia [*Henry and Wang*, 1991; *Shi et al.*, 1989] which have been primary targets of the Ocean Drilling Program (ODP) and the Integrated Ocean Drilling Program. Here the Hellenic subduction zone in the eastern Mediterranean Sea is considered where a wide accretionary complex, the Mediterranean Ridge (in the following, abbreviated as MedRidge)

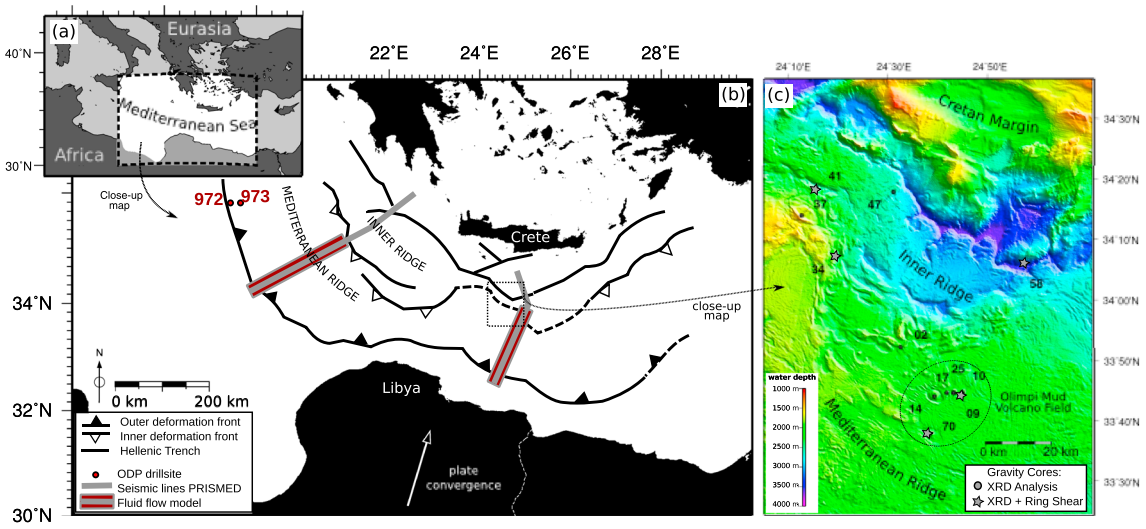

Figure 1. (a) Overview map of study area. (b) Close-up view of the eastern Mediterranean Sea showing the main tectonic features [after *Kopf et al.*, 2003], the locations, and hole numbers of two ODP (Ocean Drilling Project) drill sites [*Emeis et al.*, 1996], the location of two seismic lines shot during the PRISMED survey [*Chaumillon and Mascle*, 1997] (cross sections in Figure 2), and the location targeted by the fluid flow models. Direction of plate convergence is taken from *Le Pichon et al.* [1995]. (c) Sample region of the gravity cores taken by *Kopf et al.* [2012], which were used for the geotechnical analysis in this study. Bathymetric chart from *Huguen et al.* [2006].

has evolved since approximately 19 Ma (million years before present) [*Kopf et al.*, 2003]. Compared to other accretionary prisms, the MedRidge is outstanding due to the very thick presubduction sequence, the extremely low taper angle of the accretionary prism and the along-strike variation in geometry as a result of the incipient collision between Africa and Eurasia. The MedRidge has been studied by seismic surveys [*Mascle et al.*, 1986], swath mapping [*Huguen et al.*, 2006; *Chaumillon and Mascle*, 1997], and scientific drilling [*Emeis et al.*, 1996; *Ryan et al.*, 1973]. However, there is a lack of quantification of fluid flow processes on a regional scale.

To investigate the large-scale MedRidge hydrogeology, we set up two 2-D fluid flow models along transects perpendicular to the deformation front. We evaluated preexisting geophysical data and gathered new geotechnical data to obtain the governing input parameters for our models. The model output are the fluid pressure distribution and fluid flow directions in the prism. These parameters help to understand the distribution of observed main fluid pathways within the shallow portion of the subduction system (e.g., the prominent mud domes in the landward fore arc [*Kopf et al.*, 2001]).

2. Regional Setting

2.1. Mediterranean Ridge Accretionary Prism

The accretion of sediments in the Eastern Mediterranean Sea is a result of the subduction of the African Plate beneath the Eurasian Plate, which initiated in the late Eocene when the southern branch of the Tethys was partly closed [*Dewey et al.*, 1973]. The present-day MedRidge, which appears on bathymetric maps as a curved high between Greece and Libya (Figure 1), accumulated since only 19 Ma [*Kopf et al.*, 2003]. Materials which were underthrust and subducted to depth earlier underwent high pressure–low temperature metamorphism before getting exhumed again [*Thomson et al.*, 1998]. Those exhumed units then formed the abutment, or rigid backstop, against which off scraping took place. The growth of the accretionary complex was further affected by four main events: (1) An increase in net convergence rate between Crete and Africa from 1 cm/a to 3–4 cm/a [*Le Pichon et al.*, 1995] and subsequently an increase in rate of frontal accretion due to extensional deformation north of Crete in the Neogene that caused the initiation of back arc spreading at 13 Ma [*Pichon and Angelier*, 1979]. (2) The position of the initial backstop shifted seaward (associated with trench rollback) in the Pliocene because earlier accreted sediments had undergone sufficient dewatering and porosity loss to act as a rigid second-phase backstop (Inner Ridge) [*Kopf et al.*, 2003]. (3) Approximately 5 Ma ago the continental lithosphere of the passive continental Libyan margin reached the deformation front in the central part of the MedRidge. The ongoing collision led to an uplift and deformation of the central MedRidge and to a stagnation of wedge outbuilding rate [*Kopf et al.*, 2003]. Due to this

Table 1. MedRidge Characteristics Compared to Two Other Accretionary Prisms[a]

	MedRidge	Nankai/Japan	Barbados
Convergence rate (cm/a)	3–4 (1)	2–4 (2, 3)	2–2.2 (4)
Taper angle (deg)	~1 (5)	4–9 (6, 7)	3–5 (8)
Lithology	See sections 2.1 and 3.1	Hemipelagic mudstone (9); sand and ash turbidities (Ashizur transect (6))	Pelagic calcareous mudstone and hemipelagic clays (10)
Thickness incoming/underthrust sedimentary sequence (km)	Thick underthrust sequence in the western part, thin in the center (see Table 3)	Thin underthrust sequence (incoming: 1–1.3; underthrust: 0.3–0.45 (7)	Intermediate thick underthrust sequence: (incoming: 0.7; underthrust: 0.46 (12, 13))
Age of oceanic basement (Ma)	Old: 110–140 (14)	Young: 15–25 (15)	Intermediate: 84 (8)
Heat flow from incoming plate (mW/m^2)	16–41 (14,16)	90–240 (Muroto transect (17)), 40–60 (Kii transect (18))	40–55 (8)

[a]Numbers in parentheses refer to the following references: (1) *Le Pichon et al.* [1995], (2) *Karig and Angevine* [1986], (3) *Seno* [1977], (4) *Stein et al.* [1988], (5) *Kopf et al.* [2003], (6) *Moore et al.* [2001], (7) *Saffer and Bekins* [1998], (8) *Ferguson et al.* [1993], (9) *Taira et al.* [1992], (10) *Moore et al.* [1988], (12) *Biju-Duval et al.* [1982], (13) *Bekins and Dreiss* [1992], (14) *Sclater et al.* [1980], (15) *Kobayashi et al.* [1995], (16) *Camerlenghi et al.* [1995], (17) *Saffer et al.* [2008], and (18) *Hamamoto et al.* [2011].

collision, the MedRidge is significantly shortened in the central part south of the island of Crete [*Chaumillon and Mascle*, 1997; *Chaumillon et al.*, 1996]. (4) Finally, the shape of the MedRidge was further modified during the Messinian salinity crisis (5–6 Ma ago), when the Mediterranean Sea nearly completely dried out [*Müller and Wright*, 1977]. The western and eastern branch of the MedRidge where overlain by an evaporite layer, whereas the elevated central part remained above sea level and was partly eroded [*Chaumillon and Mascle*, 1997]. The very narrow taper angle (~1°) has been proposed to be the result of the presence of the Messinian evaporites within the wedge and along the decollement [*Kastens et al.*, 1992; *Chaumillon et al.*, 1996; *Chaumillon and Mascle*, 1997]. A decollement in salt would be characterized by very low basal shear strength and therefore favor stable sliding for a wedge with MedRidge geometry [*Logan*, 1978; *Dahlen*, 1990]. However, taking into account the period of the salinity crisis, wedge outbuilding rate and the rate of plate convergence [*Pichon and Angelier*, 1979; *Müller and Wright*, 1977], evaporite in the MedRidge accreted sediments are only present in the frontal part of the western and eastern branch of the MedRidge where evaporites are incorporated into or underthrust the accretionary complex. Large parts of the whole wedge were either formed before the Messinian or were above sea level during the peak of the crisis.

2.2. The MedRidge Compared to Other Accretionary Prisms

As a result of this unique geodynamic evolution, the MedRidge accretionary prism shows a low slope angle (~1°), >200 km width and incoming sediments exceeding 4 km in thickness in the western part. In the frontal portion of the prism the incorporation of evaporites may further affect the mechanical response and also results in rather minor heat flow from the oceanic basement. To better discriminate the influence of these factors in our model in comparison to the accretionary prisms of Nankai (Japan) and Barbados, probably two of the best studied accretionary margins, we compile the main characteristic of these systems (Table 1). Although collision features are anticipated to be enhanced in the eastern Mediterranean as a result of the proximity of the African continent, there is a remarkable number of similarities to both Nankai and Barbados. The central portion of the MedRidge has a thin underthrust section relative to the wedge (Figure 2), similar to that of, e.g., Nankai and Barbados. Heat flow is relatively low in the eastern Mediterranean because of the older oceanic (and intermediate) crust when compared to Nankai and Barbados; however, if the Muroto transect off Japan is excluded, there is broad agreement in surface heat flow as well (Table 1). With respect to fluid flow and taper angle, the central MedRidge shows similarities to the Nankai Trough Seismogenic Zone Experiment transect offshore Kii Peninsula, where fluid expulsion takes place diffusively in the high-strain zone near the toe as well as conductively further landward along high-permeability zones, as illustrated by active mud volcanoes in the Mediterranean [*Kopf et al.*, 2001] and Kumano Basins [*Kopf and Shipboard Party*, 2013], respectively. Along other profiles further east or west of the main collision zone in the eastern Mediterranean, the situation differs from Nankai and Barbados as sediment accumulation in the Ionian and Levantine Basins result in underthrust sequences of several kilometers in thickness (see Table 1, and references therein). With the modeling of this study, we hence follow a strategy where a western and central MedRidge profile serve as end-members to shed light on the effects of (i)

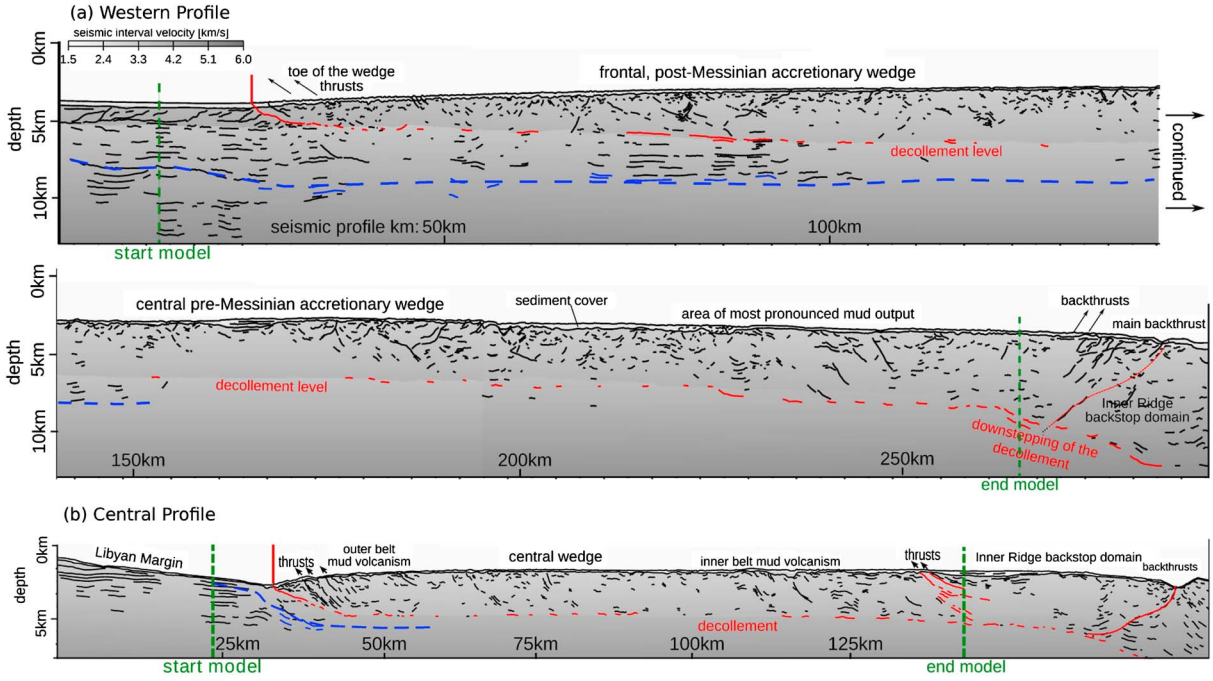

Figure 2. Interpretation of the seismic profiles along which fluid flow modeling is carried out (see map in Figure 1b for the locations). The landward and seaward model boundary are marked by a green line. The deformation front is indicated by a vertical red line. The dashed blue line indicates the sediment-basalt contrast. The grey scale gives the seismic interval velocities (modified after *Kopf et al.* [2003]). (a) Western profile and b) central profile.

accentuated collision owing to the proximity of Africa (central profile) and (ii) thick underthrust sequences (western profile) for porosity and permeability development in a wide, mature accretionary complex.

3. Model Constraints From Data

Considering the differences and similarities between the MedRidge and, e.g., Nankai or Barbados, we expect a numerical fluid flow model from the MedRidge to yield new insights in the geodynamic and hydrogeological characteristics of such margins. Preexisting seismic observations by *Kopf et al.* [2003] form the most important large-scale geometrical constraint. Additionally, to constrain further sediment properties, we undertake measurements on sediment samples from the study area (section 3.2). Apart from those primary data, we also used the geophysical information to derive basic sediment properties (summarized in section 3.1). However, those data could not be used directly for modeling but required several calibration and processing steps. The derivation of these secondary data is presented in section 4.

3.1. Preexisting Data

In order to constrain the geometry of the MedRidge accurately, our models are set up following two seismic lines that span the entire accretionary complex (Figure 2). To capture the along-strike variation in wedge geometry, one model is located in the western and one in the central part of the ridge. The interpretation of these seismic lines by *Kopf et al.* [2003] is shown in Figure 2, and the main characteristics are discussed here (see *Kopf et al.* [2003] for details) together with findings from other observations:

At the deformation front of the western MedRidge (Figure 2a) a thick sedimentary sequence (approximately 4 km) is incorporated into the prism [*Chaumillon et al.*, 1996], resulting in a high rate of seaward growth of the accretionary prism (0.5–2.0 cm/a) [*Kastens*, 1991]. The outer part of the complex consists of Plio-Quaternary sediment cover, on top of Messinian evaporites and a thick Cenozoic to Mesozoic sedimentary infill [*Chaumillon and Mascle*, 1997]. In this very frontal part, the decollement is located at the base of the evaporites. About 80 km landward from the deformation front, the accreted material consists of Miocene sediments that were accumulated before the Messinian salinity crisis [*Ryan et al.*, 1973], which are transported toward deeper levels of the subduction system [*Chaumillon et al.*, 1996]. Large mud volcano fields were detected in the central part and in the backstop region of the fore arc, which may indicate overpressured sediments in the deeper MedRidge [*Rabaute and Chamot-Rooke*, 2007].

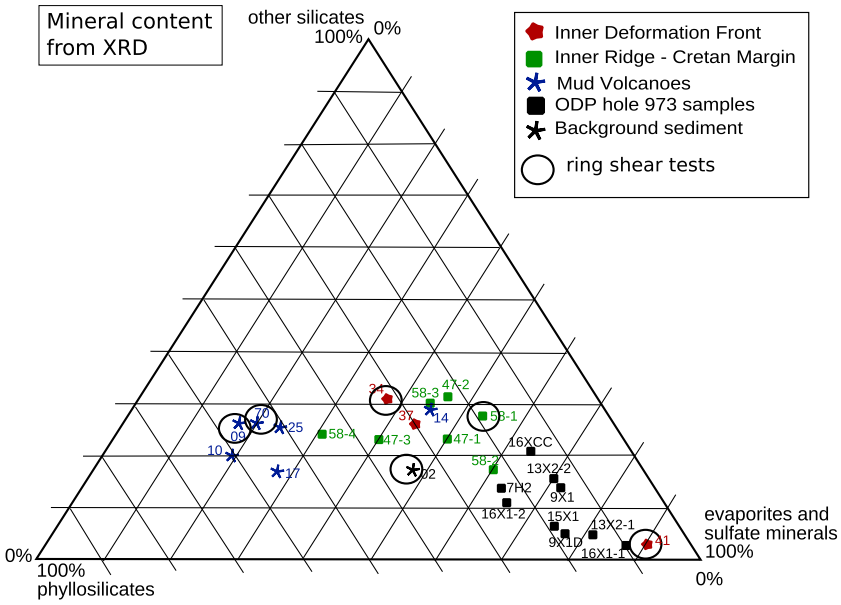

Figure 3. Results of XRD analysis (section 3.2.1). Sample location is highlighted in Figure 1c. Samples surrounded by black circles were analyzed by ring shear tests (results in Table 2).

Between Libya and Crete, the MedRidge has been significantly shortened compared to the western and eastern part (Figure 2b). The direct contact between the steep Libyan continental margin and the deformation front in the central part of the MedRidge caused an over steepened frontal zone and a back thrust movement of the whole complex over the backstop [*Kopf et al.*, 2003]. Approximately 10 km behind the deformation front, the steep outer zone transitions to a nearly flat plateau region [*Huguen et al.*, 2006], suggesting a formation by erosion when the central part was above sea level during the Messinian salinity crisis [*Chaumillon and Mascle*, 1997]. Mud volcanoes are confined to an outer zone approximately 40 km from the deformation front and an inner zone more than 100 km from the deformation front [*Camerlenghi et al.*, 1995]. Geochemical analysis of the sediment pore waters recovered at the inner mud volcano belt suggested a deep-seated origin, possibly as deep as the decollement [*Deyhle and Kopf*, 2001].

3.2. Newly Collected Data

To constrain the sediment properties, we undertook compositional and geotechnical analysis. These analyses are introduced methodologically in the next paragraphs. The associated results are also presented in this section, because the data represent a prerequisite for the main part of the paper, the numerical modeling.

Seven sediment samples originated from ODP (Ocean Drilling Program) Site 973 [*Emeis et al.*, 1996], which is located near the deformation front in the western branch of the MedRidge (Figure 1,b). The samples chosen cover a depth range between 56 and 145 m below seafloor (m bsf) and are of early Pleistocene age. Another 12 specimens were recovered by gravity coring during RV *POSEIDON* cruise P410 [*Kopf et al.*, 2012] in the backstop region at the central part of the MedRidge (Figures 1b/1c). The P410 samples studied contain specimens from the Olimpi mud volcano field (approximately 120 km north of the deformation front) and also the Inner Ridge and backstop region, where deep-seated mud is lubricating the back thrust faults [*Deyhle and Kopf*, 2001]. Consequentially, the ODP Site 973 samples are more representative for shallow regimes of the MedRidge, in particular the frontal region of the prism, whereas the P410 samples are likely to have a deeper origin and older age. Although dating has not been carried out and depth estimates from illite crystallinity give a range from 3 to 6 km (depending on assumed thermal gradient), we take these materials as representative for the older and deeper strata of the MedRidge.

3.2.1. X-Ray Diffraction Analysis to Constrain the Sediment Mineral Content

The XRD (X-ray diffraction analysis) measurements were undertaken using a Philips X'Pert Pro multipurpose diffractometer and were analyzed using the software package QUAX [*Vogt et al.*, 2002]. The results (Figure 3) reveal that the ODP samples from the toe of the western MedRidge are dominated by evaporites and sulfate minerals (average of 73%), whereas the percentage of clay minerals is generally low (average of 16%). In contrast, seafloor samples taken from regions near active mud volcanoes are clay dominated

Table 2. Mean Value of the Residual Coefficient of Friction (μ[a]) From the Sediment Samples Highlighted in Figure 3

Sample Number	Applied Normal Stress (MPa)						
	0.2	0.4	0.8	1.6	3.8	7.6	15.2
				μ =			
41	0.62	0.61					
02		0.59	0.58				
58			0.40	0.43	0.44	0.34	0.34
09				0.29			
34				0.27	0.24	0.24	
70				0.28	0.16	0.20	

[a]The residual coefficient of friction (μ) was measured using a ring shear apparatus at a shear velocity of 0.06 mm/min. Uncertainty of μ is in the range of $\pm$0.002.

(average of 48%). Samples from the Inner Ridge and backstop domain have approximately half the clay content (average of 22%) of the mud volcano samples. These results are consistent with the hypothesis that the central MedRidge was unaffected by the deposition of evaporites during the salinity crisis [*Chaumillon and Mascle*, 1997]. Assuming that the sediments expelled at the mud volcanoes in the central MedRidge rise from depth, the deep regions of the MedRidge could be more clay dominated than the shallower regions. This is supported by the results from hemipelagic background sediments (average 25–35% clay minerals), which were recovered in P410 gravity cores taken next to the mud volcano field [*Kopf et al.*, 2012].

3.2.2. Ring Shear Experiments to Constrain the Sediment Shear Strength

We further undertook ring shear tests to quantify the coefficient of friction (μ) of the sediments, which will be used in section 6.2 for critical taper analysis. Ring shear test were run using selected P410 sediment samples from gravity coring [*Kopf et al.*, 2012]. A Wykeham-Farrance ring shear apparatus was employed to measure the peak shear strength and drained residual strength of seawater-saturated specimens. Details regarding the equipment and procedure may be found in *Minning et al.* [2006]. In our study, data were acquired using a constant shearing velocity of 0.06 mm/min at normal stresses up to 15.2 MPa. Although we see some changes in friction coefficient with effective stress, the resulting residual friction coefficients can be clearly grouped in two subsets of low ($\mu = 0.16$–0.45) and moderately high ($\mu = 0.53$) friction coefficients (see Table 2): The first group encompasses all mud volcano samples and those samples from the Inner Ridge that had a similar composition as revealed by the XRD analysis. The second group comprises the samples with lower clay content, either from hemipelagic background sedimentation (P410 sample 02) or the toe of the western MedRidge (ODP Site 973). This lithological dependency regarding clay mineral content suggests different mechanical domains of the MedRidge. Assuming that the mud volcano samples originate from greater depth we simplistically infer that the accretionary wedge consist of a deeper, clay-dominated, frictionally weak domain near the decollement and a shallower less clay-dominated, stronger domain within the upper accreted sediments.

4. Numerical Modeling

For the hydrogeological model of the accretionary complex, we use a two-dimensional steady state numerical approach, which is justifiable assuming that model parameters change most severely with distance from the deformation front and with depth [*Saffer and Bekins*, 2006]. We assume the wedge geometry to be constant over time, which is consistent with a sedimentary prism at Coulomb failure [*Davis et al.*, 1983]. Accordingly, the steady state simulations deliver results that represent the long-term maintenance of a critical taper. Fluid flow is calculated using a steady state flow equation based on the combination of the conservation of mass and Darcy's law [*Voss and Provost*, 1984]:

$$\mathrm{div}\left[-\frac{\underline{\mathbf{k}}}{\eta}(\mathrm{grad}\,P - \rho_f \mathbf{g})\right] - Q = 0 \tag{1}$$

where $\underline{\mathbf{k}}$ is the intrinsic permeability tensor, η is the dynamic viscosity of the fluid, P is the fluid pressure, ρ_f is the fluid density, $\mathbf{g}$ the gravitational acceleration, and Q is a fluid source term. The first term in equation (1) accounts for the fluid flow in and out of an element in the model, whereas the second term (Q) accounts

Table 3. Model Geometry for Numerical Modeling[a]

	Western Profile		Central Profile		
Vertical model extend	at deformation front	at backstop	at deformation front		at backstop
Prism	1.5 km	4.04 km	0.56 km		3.86 km
Decollement	0.02 km		0.02 km		
Underthrust	4.8 km		0.5 km		
Horizontal model extend	250 km		120 km		
Wedge angles	10–140 km	140–250 km	10–20 km	20–110 km	110–120 km
α[b] (deg)	0.57	−0.90	4.8	0	−3.2
β[c] (deg)	0.55	0.90	10.47	0.28	3.2
Water depth at deformation front:	4000 m			3270 m	

[a]The geometry is adopted from the seismic lines in Figure 2. The wedge thickens with distance from the deformation front, whereas the thickness of the decollement and the underthrust sediments is constant.
[b]Surface slope (α).
[c]Decollement dip (β).

for fluids released by sediment compaction (section 4.4.1) and clay dehydration (section 4.4.2). Equation (1) is solved using a slightly modified version of the computer code SUTRA [*Voss and Provost*, 1984]. Changes are incorporated to include the temperature dependency of fluid viscosity and density. We used empirical relations by *Voss and Provost* [1984] and by *Sun et al.* [2008], respectively. Equation (1) is solved elementwise within the given model geometry (Table 3 and Figure 4), having deduced the input parameters and taking into account the boundary conditions. The flow chart in Figure 5 summarizes the most important model parameters and model steps. The model outputs are fluid pressure and flow velocity. We also carry out a sensitivity analysis for the sediment permeability because no in situ measurements are available for the MedRidge to constrain this parameter.

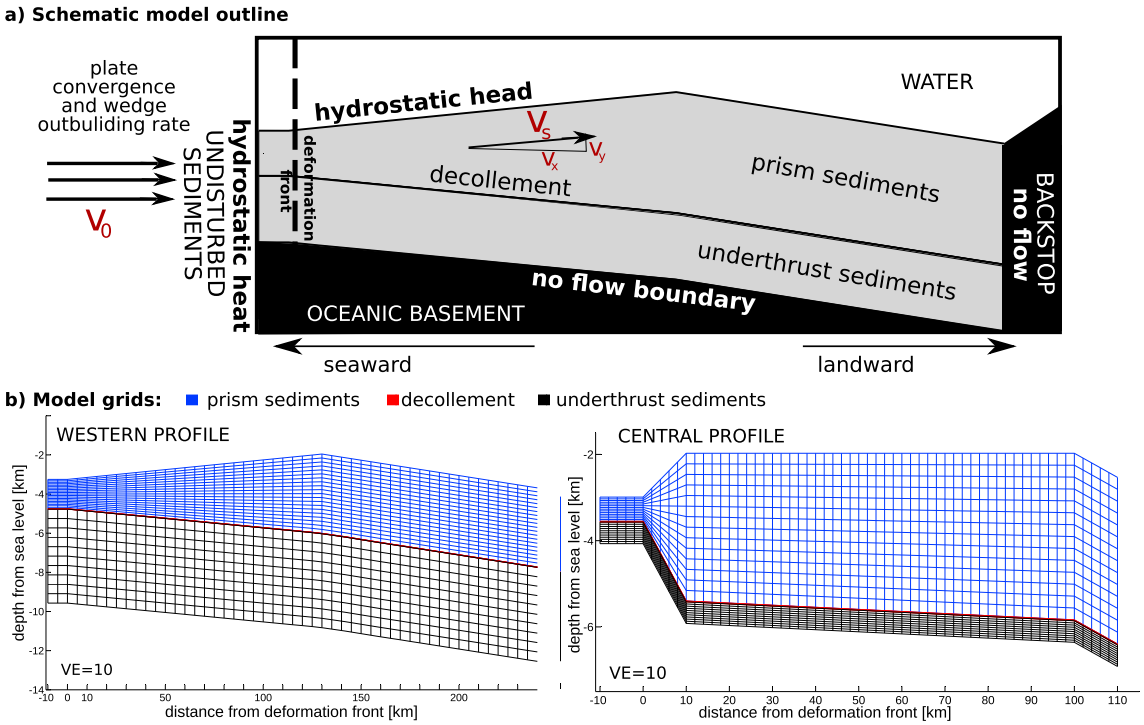

Figure 4. (a) Schematic model outline (gray area) and boundary conditions for numerical modeling. The model geometry is constant over time and fixed to the deformation front. The sediment velocity V_s has a vertical (V_y) and a horizontal (V_x) component within the wedge. V_0 is the initial sediment velocity at the deformation front. (b) Grid spacing of the two models (exact model characteristics are listed in Table 3).

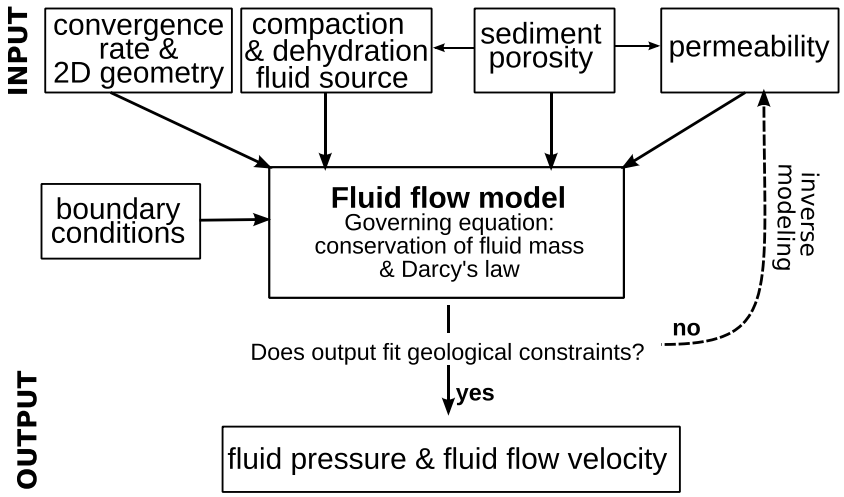

Figure 5. Relation between the different model parameters. The permeability is constraint interactively by a sensitivity analysis (section 5.2).

4.1. Model Domain

The two numerical models are orientated along the seismic lines as shown in Figure 2. Both profiles are orientated perpendicular to the deformation front and extend from 10 km outboard of the deformation front to the backstop. Based on the seismic profile the model is separated into the wedge, the decollement, and the underthrust sequence (see Figure 4 for the schematic model outline and Table 3 for the exact values). As the sediment/basalt contrast cannot be resolved near the backstop by the seismic data but remains relatively constant in the resolved area, we assume that the underthrust section thickness is conserved further away from the deformation front, too. The models are subdivided in 1700 and 1680 elements for the western and central profile, respectively, with the model coordinate system fixed to the deformation front (see Figure 4b). The single elements have unique hydrogeological characteristics and are quadrilateral with nodes at the four corners. Final modeling results are interpolated linearly between the nodes. The top and the seaward model boundaries are hydrostatic constant pressure boundaries, assuming that the incoming sequence is undisturbed seaward of the deformation front. The landward and bottom model boundaries are no-flow boundaries based on the assumption that sediments become impermeable as a result of advanced compaction at the backstop and at the sediment-crust contact, respectively [*Saffer and Bekins*, 1998].

Compaction of sediment is determined by tracking the movement of sediment packages through the model domain. Packages of water-saturated sediments enter the model domain at the deformation front at a constant initial velocity (V_0), which is orientated horizontally. The packages then follow lines of constant convergence within the model domain. Due to the thickening of the wedge, the horizontal velocity component (V_x) is slowed down, and the absolute value of the vertical velocity component (V_y) increases, dependent on the position in the model domain and the taper angle. In the current model geometry, the taper angle changes with distance to the deformation front, which allows to mimic the true geometry of the accretionary complex, and yields more realistic values for velocities than assuming a constant taper angle in the model domain. To constrain the initial horizontal velocity with which the sediments enter the model domain, an average value since the onset of accretion is employed. The sum of net convergence normal to the deformation front and the wedge outbuilding rate is 3.61 cm/a in the central MedRidge, where frontal accretion stagnates since the initiation of collision with the Libyan margin [*Dewey et al.*, 1973; *Le Pichon et al.*, 1995; *Kastens*, 1991]. In the western MedRidge, the plate movement is orientated obliquely to the deformation front [*Le Pichon et al.*, 1995], but outbuilding of the prism has taken place at very fast rates for the past 19 Ma [*Kopf et al.*, 2003]. We deduce an average horizontal movement of 3.5 cm/a since 19 Ma before present.

4.2. Sediment Porosity

In our model approach, permeability and the compactional fluid source are constrained from porosity and porosity gradients in the accretionary prism, respectively. Sediment porosity is therefore one of the most

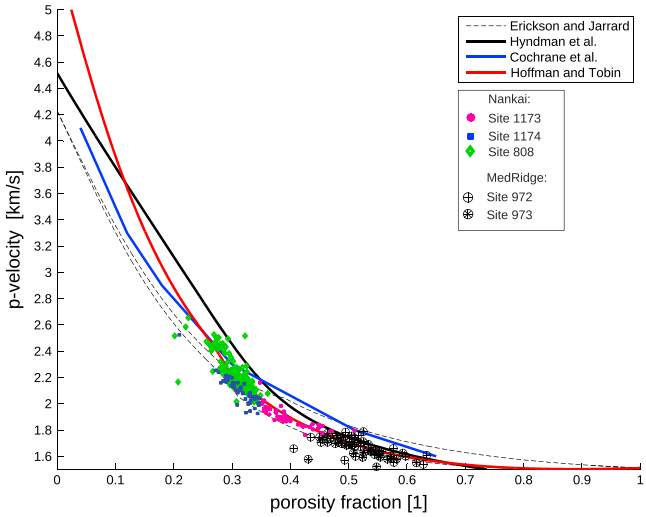

Figure 6. Different velocity-porosity relationships for sedimentary prisms: The *Cochrane et al.* [1994] relation was used for the Oregon Accretionary Complex. *Hyndman et al.* [1993] and *Hoffman and Tobin* [2004] derived relations for the Nankai accretionary complex. The *Erickson and Jarrard* [1998] relation is a global velocity-porosity relation which was used by *Hoffman and Tobin* [2004] for Nankai for normally (lower curve) and highly consolidated (upper curve) material. Nankai data points are from three boreholes up to 10 km from the deformation front [*Hoffman and Tobin*, 2004]. MedRidge data are in situ corrected values from ODP measurements.

important input parameters. Porosity generally decreases with depth and distance from the trench [*Bray and Karig*, 1985], and several authors made use of this observation to approximate the porosity distribution of an accretionary complex in numerical fluid flow models assuming an exponential porosity decay with depth [e.g., *Bekins and Dreiss*, 1992; *Saffer and Bekins*, 1998].

Here we aim to capture finer variations of porosity within the model domain. This is achieved by using observations from drilling and seismic reflection data and interpolating these values directly into our model domain. *P* wave seismic interval velocities reported by *Kopf et al.* [2003] (Figure 2, gray scale) are available for the entire area that is captured by our model domains. Compared to the spatially scarce data from core materials, the seismic interval velocities represent the most important large-scale information which can be used to constrain sediment porosity.

4.2.1. Derivation of Sediment Porosities

To establish an empirical relation between these seismic compressional (*P* wave) velocities and sediment porosities, we use available shipboard measurements from ODP Site 973 at the toe of the MedRidge [*Emeis et al.*, 1996] for calibration. We have taken into account the different factors that impact seismic velocities and shipboard measurements on sediments: shipboard measured porosities are generally too high and velocities too low, because sediments experience expansion during unloading. Furthermore, compressional wave velocities measured in boreholes were systematically smaller than the seismic interval velocities. This offset arises due to the different wavelengths that are used for the measurement [*Costa Pisani et al.*, 2005]. To account for these effects, first, the *Emeis et al.* [1996] shipboard porosity and velocity measurements were corrected for rebound effects. To quantify the amount of porosity expansion the rebound curve from oedometer tests (Table 2, sample 41) was used. Applying the rebound correction to the ODP shipboard porosity measurements, results in a porosity decrease of 0.021 (i.e., ~2%) at 120 m bsf.

Regarding the correction for compressional wave velocities, shipboard-core measurements and borehole in situ measurements were available at ODP Site 973 at a depth range from 52 to 66 m. The velocity rebound correction was calculated by fitting a straight line to the residuals between these two measurements assuming similar velocities at the sea bottom [*Urmos et al.*, 1993]. The regression line has a slope of 0.56 1/s resulting in a velocity rebound correction of 56 m/s at a depth of 100 m.

The result of the two corrections described above are pseudo in situ porosities and compressional velocities. These rebound-corrected MedRidge data points were then compared to established empirical relationships between compressional wave velocity and sediment porosity for marine sediments [*Erickson and Jarrard*, 1998] and accretionary prisms [*Cochrane et al.*, 1994; *Hoffman and Tobin*, 2004]. All these relations

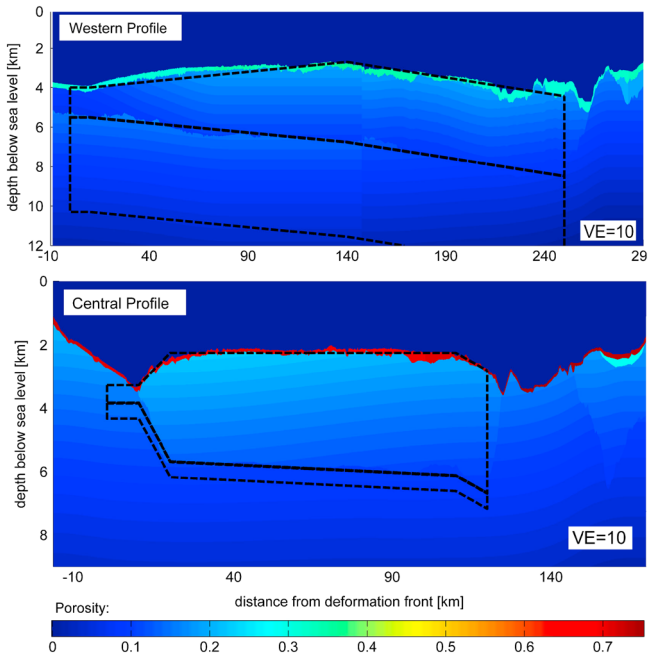

Figure 7. Sediment porosity distribution within the MedRidge gained from corrected seismic interval velocities using an empirical conversion relation by *Hoffman and Tobin* [2004]. The dashed lines represent the model outline. In the lowermost part of Profile 03, where no seismic data are available, the porosity is set to a constant value (0.01). The sudden porosity jump in profile PM03 at 150 km is also reflected in the seismic velocities but has a minor effect on the absolute porosity values. The salt water on top of the sediments is dark blue (VE = vertical exaggeration).

follow a common trend of increasing velocity with decreasing porosity (Figure 6). Porosities of the corrected MedRidge measurements (Figure 6, black dots) seem to agree best with data from the Nankai subduction zone, so that we used the *Hoffman and Tobin* [2004] relationship, initially established for the Nankai margin, for the MedRidge as well:

$$n = -1.180 + 8.607\, v_p^{-1} - 17.89\, v_p^{-2} + 13.94\, v_p^{-3} \tag{2}$$

where n is the porosity and v_p (km/s) the compressional wave velocity. There are also fundamental differences between local borehole measurements and larger-scale seismic-derived velocities that have to be accounted for. The seismic interval velocities published by *Kopf et al.* [2003] were generally higher than the rebound corrected borehole measurements at ODP Site 973. Since the latter are more meaningful for our model approach, we reduced the seismic interval velocities systematically by 180 m/s to achieve an overlap between both data sets at the location of ODP Site 973. After this reduction, the seismic interval velocities could be converted to porosity values using equation (2).

The calculated sediment porosity distribution is plotted in Figure 7. In both profiles, the low-porosity accreted strata are overlain by a high-porosity sedimentary cover. Beneath the sedimentary cover, porosities decrease with depth gradually. However, the intensity of decrease varies nonlinear with distance from the deformation front. Moreover, porosities in the underthrust section of the western profile are higher than at the bottom of the wedge, and a jump in porosity appears at kilometer 145. Using these porosities to derive an empirical porosity(n)-depth(z) decay function [e.g., *Athy*, 1930], we gain

$$n = 0.218 \cdot e^{-0.228 \cdot z};\ R^2 = 0.624 \text{ for the western profile} \tag{3}$$

$$n = 0.228 \cdot e^{-0.255 \cdot z};\ R^2 = 0.646 \text{ for the central profile} \tag{4}$$

However, these fits have relatively low R^2 values, which arise due to the complexities in porosity field described above. In contrast to previous studies where the computed porosities were used to derive an empirical function, we choose to fit the resulting porosity distribution directly into the model geometry. The

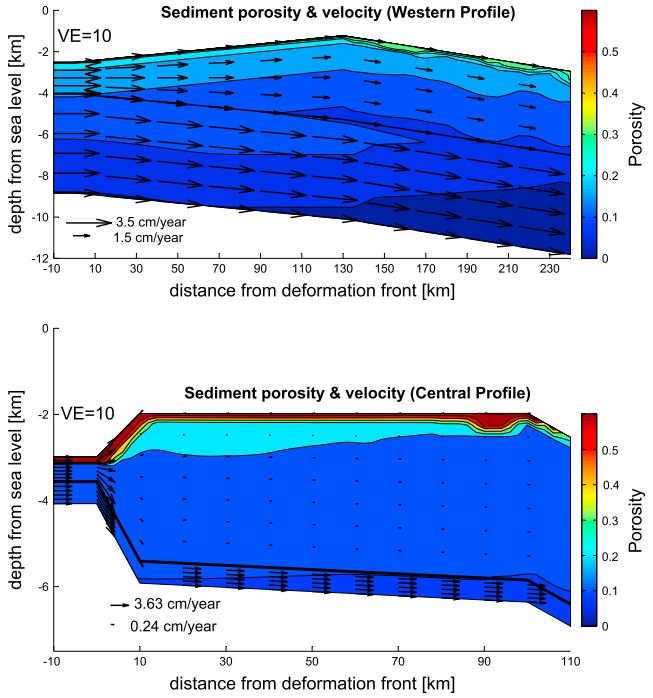

Figure 8. Porosity distribution in the model domain derived from the conversion of seismic interval velocities to sediment porosity (section 4.2). Sediment velocities (V_s) are calculated assuming that they follow lines of constant convergence (equations (7) and (8)) (VE = vertical exaggeration).

transformation from real to model geometry was carried out considering two criteria: The model geometry and the geometry from seismic reflection data had to overlap at the decollement and at the sea bottom. The porosities from the seismic data were transferred columnwise to the model grid. Finally, the porosity distribution in the model domain was smoothed by averaging over twice the model node distance in order to avoid the introduction of artifacts due to the transformation. In the frontal part of the western profile, the seismic interval velocities decrease with distance from the deformation front, resulting in a porosity increase. This circumstance cannot be explained by any geological processes. Therefore, to avoid the introduction of geologically unrealistic parameters in the model, the first 140 km of the wedge were represented by the exponential decay curve of the western profile rather than directly by the converted porosities.

The resulting sediment porosities (Figure 8) generally decrease with burial depth; however, they also show some changes with distance from the deformation front, which would be hard to capture using an exponential decay function alone. Porosities are highest at the ocean bottom ($n = 0.72$ for the central and $n = 0.36$ for the western profile) and decrease rapidly at the transition between cover sediment and accreted sediment. Within the accreted wedge sediments, porosity decreases steadily with depth. In the western profile, the elevated porosity of the underthrust sediments diminishes at a distance of ~140 km landward of the deformation front. Average sediment porosities in the accreted strata are 0.22 and 0.16 in the central and western profile, respectively. Computed porosity values in the MedRidge are generally lower than those from the Nankai accretionary prism [e.g., *Saffer and Bekins*, 1998]. This observation is consistent with differences in seismic interval velocities from these two regions. Higher-interval velocities in the MedRidge may reflect the advanced compaction caused by the thick sediment package along the western profile, lower sediment accumulation rates in the eastern Mediterranean, or more advanced lateral shortening as a result of initiation of continent-continent collision given the proximity of the Libyan promontory in the central profile. Further, the low porosity values we inferred for the deeper prism are in good agreement with the strength in friction coefficients (see section 3.2.2) and marly shales, dolomites, and sands, which were discovered by Deep Sea Drilling Project (DSDP) drilling (DSDP 13, Site 126/129) [*Ryan et al.*, 1973] below the Messinian salt.

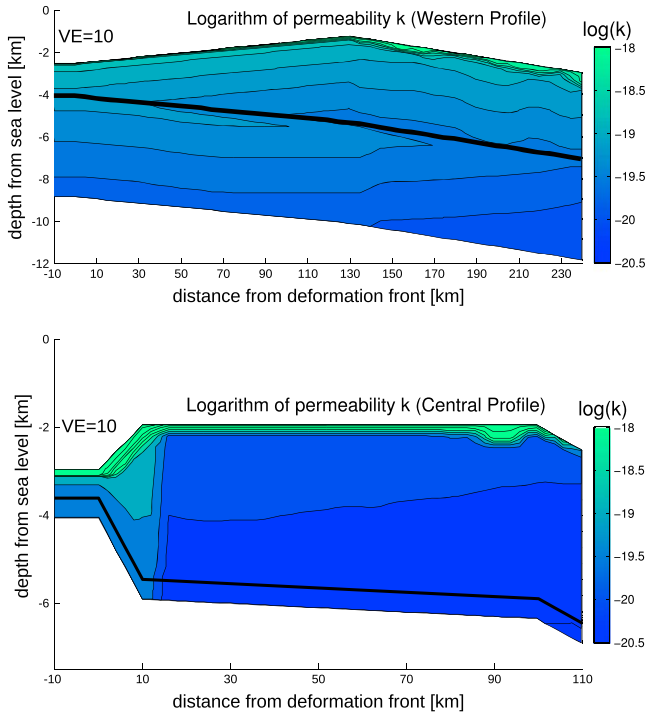

Figure 9. Permeability distribution (in log(k); k in (m^2)) inferred from sediment porosity. Parameters for the western profile: $\log(k) = 6 \cdot n - 20$; parameters for the central profile: $\log(k) = 6 \cdot n - 21$ (parameters are deduced during the sensitivity analysis in section 5.2).

4.3. Permeability

Sediment permeability affects the build up of fluid pressure because it controls the drainage capability of the sediment. Porosity and permeability can be correlated in a log-linear relationship [*Neuzil*, 1994]:

$$\log(k) = \gamma \cdot n + \log(k_0) \tag{5}$$

where k (m^2) is the intrinsic permeability and γ [1] and k_0 (m^2) are two parameters that describe the dependency between porosity and permeability. We used equation (5) to constrain the permeability in the wedge and underthrust sediments. Because we consider the MedRidge as a long-term feature, the permeability values represent an average of the matrix sediment and the fault zones in the wedge. For the central model domain a distance-dependent term is further introduced in the porosity-permeability relationship ($\gamma \cdot n + (logk_0 + 1)$ for $x < 20$ km). This is necessary because the taper angle in the frontal part of the central model is significantly over steepened due to the incipient continent-continent collision. Therefore, additional fracture zones at the toe of the complex develop that are likely to channelize flow and therefore cause an overall increase in permeability. This is accounted for by the different permeability-porosity relationship at the frontal 20 km of the complex. The permeability along the decollement (k_d) is assigned separately in order to describe the different permeability along a pronounced fracture zone [*Bekins et al.*, 1995]. The values for the parameters k_d, k_0, and γ will be evaluated in section 5.2. Figure 9 shows the permeability distribution within the model domains that was later used to calculate the fluid pressure (in section 5.3).

4.4. Fluid Sources

4.4.1. Compaction Source

The rate of fluid production by sediment compaction depends on the velocity at which the sediments migrate landward and on the porosity change along this travel path. Assuming a time-invariant porosity distribution and the conservation of fluid and solid mass, the fluid source due to compaction-induced porosity loss within the model domain can be calculated from the divergence of the sediment velocity field [*Bekins and Dreiss*, 1992] as

$$Q = \operatorname{div} \mathbf{v}_s = \frac{1}{1-n} \cdot \left(V_x \cdot \frac{\partial n}{\partial x} + V_y \cdot \frac{\partial n}{\partial y} \right) \approx \frac{1}{1-n} \cdot \left(V_x \cdot \frac{\Delta n}{\Delta x} + V_y \cdot \frac{\Delta n}{\Delta y} \right) \tag{6}$$

where n is the sediment porosity and Q is the resulting source in $\text{Volume}_{\text{fluid}}/\text{Volume}_{\text{bulk}} \cdot \text{s}$. V_s are the sediment velocity vectors plotted in Figure 8. V_x and V_y are the associated horizontal and vertical component at a model node [*Bekins and Dreiss*, 1992]

$$V_x = V_0 \cdot \frac{z_0}{z} \cdot \left(\frac{1-n_0}{1-n}\right) \tag{7}$$

$$V_y = (\tan\alpha - \frac{z_0}{h_0}(\tan\alpha + \tan\beta)) \cdot V_x \tag{8}$$

where V_0 is the initial sediment velocity, n_0 and z_0 are the porosity and the depth, respectively, at which a sediment package enters the prism at the deformation, $z = z_0 \cdot (1 + x/h_0(\tan\alpha + \tan\beta))$ is the depth of this package at some distance to the deformation front. The total height of the wedge or of the underthrust sediments at the deformation front is h_0. At the x location where the taper angle changes, the velocities were calculated under the assumption that the absolute sediment velocity landward and seaward of the kink is constant. To calculate the fluid source term by compaction, we approximated the partial derivatives in equation (6) by calculating the change of porosity with distance ($\frac{\Delta n}{\Delta x}$ and $\frac{\Delta n}{\Delta y}$).

Although we calculated the compaction fluid source in general from equation (6), we did exclude the source terms locally under certain circumstances to ensure that the model input was geologically meaningful: First, we did not include fluid sources in our model that would arise from sediments with a porosity smaller than 0.09. In the depths where the sediments reach such small porosities, the porosity loss cannot be exclusively explained by compaction [*Bray and Karig*, 1985]. Second, within the wedge, we did not include fluid sources that originate from further than 120 km behind the deformation front. This threshold is applied because the sediments that are accreted in the wedge undergo severe thickening, and the compaction-induced fluid release within the wedge is expected to stagnate at greater distances from the deformation front [*Bekins and Dreiss*, 1992]. Finally, we excluded fluid sources that originate from a very rapid porosity change with depth ($dn/dy > 10^{-14}$ 1/m). Such high rates are unrealistic for compaction driven porosity change and arise more likely from lithological contrasts, e.g., at the transition between cover sediments and accreted strata.

4.4.2. Dehydration Source

The sediments that are incorporated into an accretionary complex are fluid saturated with additional water bound in hydrous clay minerals of the smectite group. We considered the smectite-to-illite reaction that initiates at a temperature of $\approx 60°C$ [*Pytte and Reynolds*, 1988]. The change of smectite ratio with time was calculated using an empirical derived sixth-order expression following *Pytte and Reynolds* [1988]. This equation was derived by fitting observed reaction processes from a wider range of geological settings and thermal histories and is therefore applicable for sediments from the MedRidge:

$$\frac{\partial S}{\partial t} = -Ae^{-E/RT} \cdot \frac{[K^+]}{[Na^+]} \cdot S^5 \tag{9}$$

where S is the mole fraction of smectite in mixed layer illite-smectite. $A = 5.2 \cdot 10^7$ 1/s is a frequency factor, $E = 1.38 \cdot 10^5$ J/mol the activation energy, and R (in [J/mol·K]) is the gas constant. The ratio [K+]/[Na+] was assumed to be in equilibrium with K-Feldspar and temperature (T) dependent ($[K+]/[Na+] = 74.2 \cdot e^{2490/T}$) [*Pytte and Reynolds*, 1988]. To calculate the fluid release from the smectite transformation reaction, we followed *Saffer et al.* [2008], where the rate of fluid production (Γ in $\text{Volume}_{\text{fluid}}/\text{Volume}_{\text{bulk}} \cdot \text{s}$) is given by

$$\Gamma = \frac{\partial S}{\partial t} \cdot \Upsilon \cdot \Psi \cdot (1-n) \tag{10}$$

where Υ is the volumetric water content of smectite and Ψ is the volume fraction of bulk sediment composed of illite-smectite mixed layer clay. An initial value of $\Psi = 0.2$ for smectite at the deformation front was used based on the XRD results at Site 973. We further assumed that the temperatures at the deformation front are still too small to initiate the smectite-illite reaction [*Saffer and Bekins*, 1998]. A volumetric water content of 40% for smectite and 45% of detrital smectite from unreacted Miocene strata was assumed [*Steurer and Underwood*, 2003]. The exposure time was calculated using the sediment velocities within the model domain (Figure 8). To constrain the temperature in the MedRidge we used a finite difference model written by *Ferguson et al.* [1993] for the specific thermal regime of an accretionary system. In this model, the

Table 4. Model Parameters for Temperature Calculation[a]

	Fluid Phase	Solid Phase	Oceanic Basement
Conductivity (W/m°C)	0.67	4	3.1
Density (kg/m^3)	1004	2700	3330
Specific heat (J/kg°C)	4180	1000	1200
	Further properties:		
Basal fluid pressure	λ_b		0.98
Basal coefficient of friction[b]	μ_b		0.3
Wedge fluid pressure	λ		0.7
Wedge coefficient of friction	μ		0.6
Heat flow from oceanic crust[c]			38 mW/m^2
Ocean bottom temperature[d]			12°C
Radiogenic heating			$0.5 \cdot 10^{-6}$ mW/m^2

[a]Using a finite-difference model by *Ferguson et al.* [1993].
[b]Frictional properties are average values from the ring shear experiments (section 3.2.2).
[c]Basement heat flow is an average from *Sclater et al.* [1980] and *Camerlenghi et al.* [1995].
[d]Ocean bottom temperature is an average from the measurements of *Emeis et al.* [1996] and *Kopf et al.* [2012]. The other parameters are similar to *Ferguson et al.* [1993].

main parameter affecting the temperature regime is the heat flow from the oceanic crust, which is well constraint in the Mediterranean region and was assumed to be 38 mW/m^2 [*Sclater et al.*, 1980; *Camerlenghi et al.*, 1995]. Table 4 summarizes further model parameters. The resulting temperatures (Figure 10) in the model domain are not higher than approximately 120°C/km, which is reasonable considering the old age of the oceanic crust in the Mediterranean (270 to 230 Ma) [*Müller et al.*, 2008]. Figure 11 shows the gradients of the computed temperature distribution. Modeling yields temperature gradients of approximately 6 to 7°C/km. If a heat flow of 38 mW/m^2 is assumed, the temperature window for smectite to illite transformation is only reached in a fraction of the wedge sediments along the western profile.

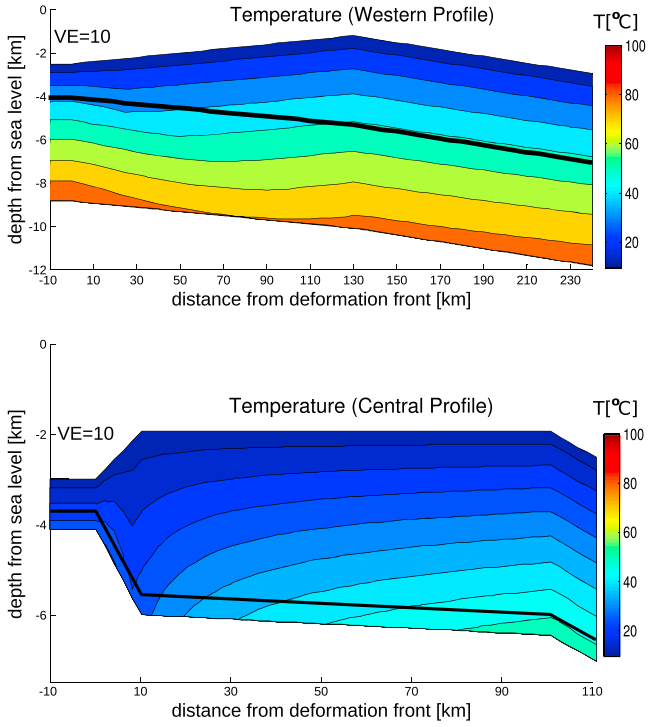

Figure 10. Temperature distribution within the model domain computed using a numerical heat flow model [*Ferguson et al.*, 1993]. Input parameters are listed in Table 4.

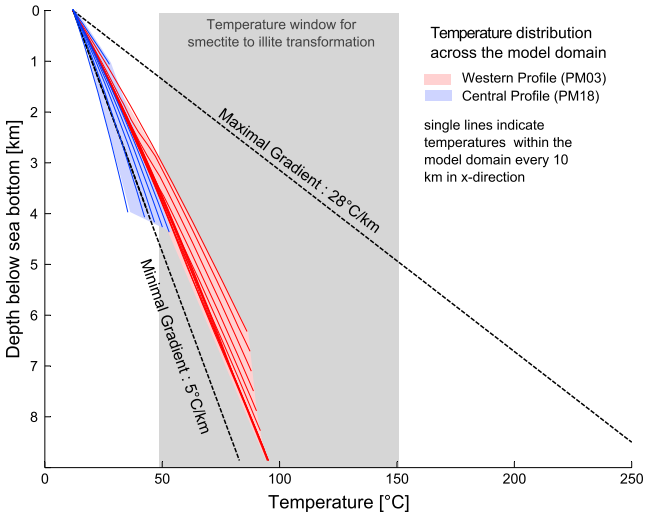

Figure 11. Temperature gradients within the model domain computed using a numerical heat flow model [*Ferguson et al.*, 1993]. Input parameters are listed in Table 4. The dashed lines represent maximum and minimum thermal gradients measured during drilling [*Emeis et al.*, 1996] and coring [*Camerlenghi et al.*, 1995]. The grey-shaded area is the area where smectite-to-illite transformation is inferred to take place [*Moore et al.*, 2007].

5. Results

5.1. Fluid Sources

For both profiles, the calculated compaction source exhibits two areas of maximum fluid production. One is located at the base of the wedge and one is located farther to the backstop within the underthrust sediments (Figure 12). The first peak arises because the velocity is highest, and porosity gradients are steepest

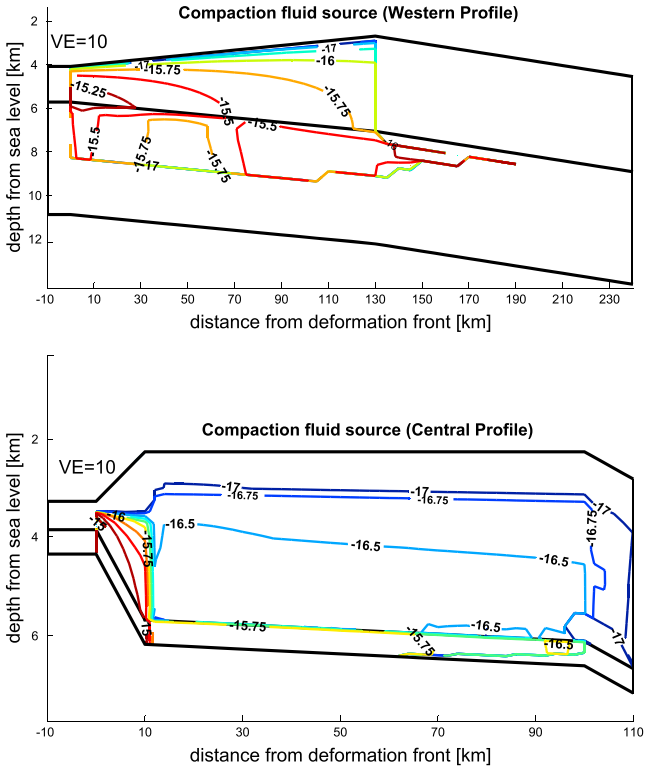

Figure 12. Contour plot of the compaction fluid source (in $\log(\text{Volume}_{\text{fluid}}/\text{Volume}_{\text{bulk}} \cdot s)$) for the porosity distribution and the velocities shown in Figure 8 calculated using the method of *Bekins and Dreiss* [1992]. The bold black line within the model domain represents the decollement.

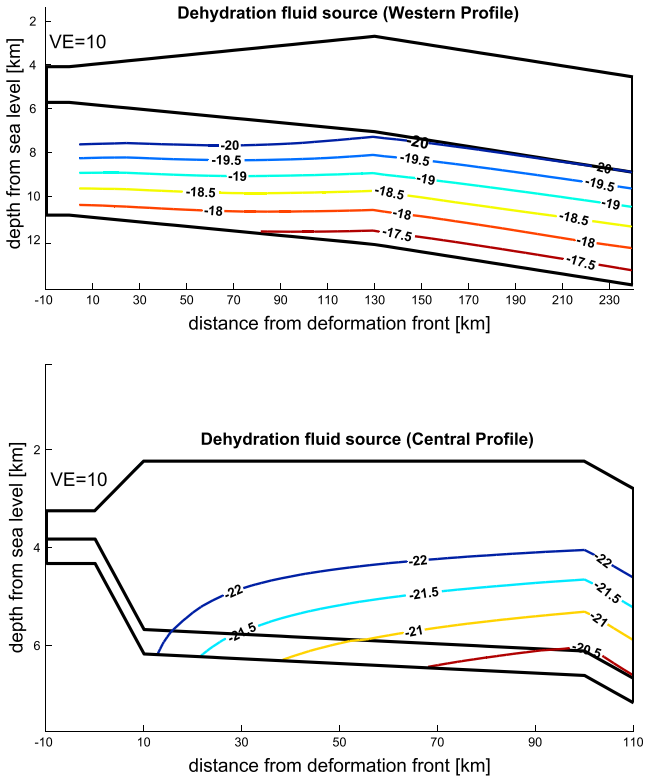

Figure 13. Contour plot of the dehydration fluid source (in $\log(\text{Volume}_{\text{fluid}}/\text{Volume}_{\text{bulk}} \cdot \text{s})$) calculated using equations (9) and (10) and the temperature distribution shown in Figure 10. The bold black line within the model domain represents the decollement.

near the deformation front, which is in agreement with large strains and fluid-laden trench sediments in that region (see below). In the underthrust sediments, fluid transport to depth is relatively fast because the sediment velocities are not slowed down as a function of wedge thickening. In our model, this leads to a shift in peak fluid production toward the backstop. Generally, the evolution of compaction fluid source is not a smooth function, because the main factor influencing the evolution of compaction source is the change in porosity between the model nodes. For example, in the underthrust section of the western profile, the change in porosity is more intense between 70 and 130 km than between 30 and 65 km. This results in a higher source term in the first case. The relatively high source term at approximately kilometer 150 results from the abrupt change in porosity at this distance (which is also visible in the seismic interval velocities). Presumably, this change would be smoother in reality than captured by the model nodes. Nevertheless, the high value of compaction source term there reflects a prominent change in sediment properties at this distance. Peak production in the western profile is 9.5^{-16} $\text{Volume}_{\text{fluid}}/\text{Volume}_{\text{bulk}} \cdot \text{s}$ in the underthrust sequence approximately 150 km landward from the deformation front. The maximum values of up to 9.1^{-16} $\text{Volume}_{\text{fluid}}/\text{Volume}_{\text{bulk}} \cdot \text{s}$ in the wedge occur at the deformation front. In the central profile the effect of the change in taper angle on the compaction source is very pronounced. Fluid production is highest in the frontal 10 km where the taper angle is steep and the sediment velocities are high. The highest value of fluid production is 6.4^{-15} $\text{Volume}_{\text{fluid}}/\text{Volume}_{\text{bulk}} \cdot \text{s}$, occurring at the deformation front just above the decollement. Landward of 20 km behind the deformation front, the compaction source term is significantly smaller than in the steep frontal part. This smaller source term in the wedge occurs because the sediment velocities are relatively low and the porosity change with distance is small.

Note here that some of the initial pore water in the underthrust deposits may be trapped beneath Messinian evaporites in the frontal portion of the western profile; this is not accounted for in our model since there is no direct evidence that such evaporites really exist at depth. In essence, it would lead to somewhat lower compaction sources in the toe area, but higher values toward the hinterland (but restricted to the frontal 50 to 75 km where evaporites may exist).

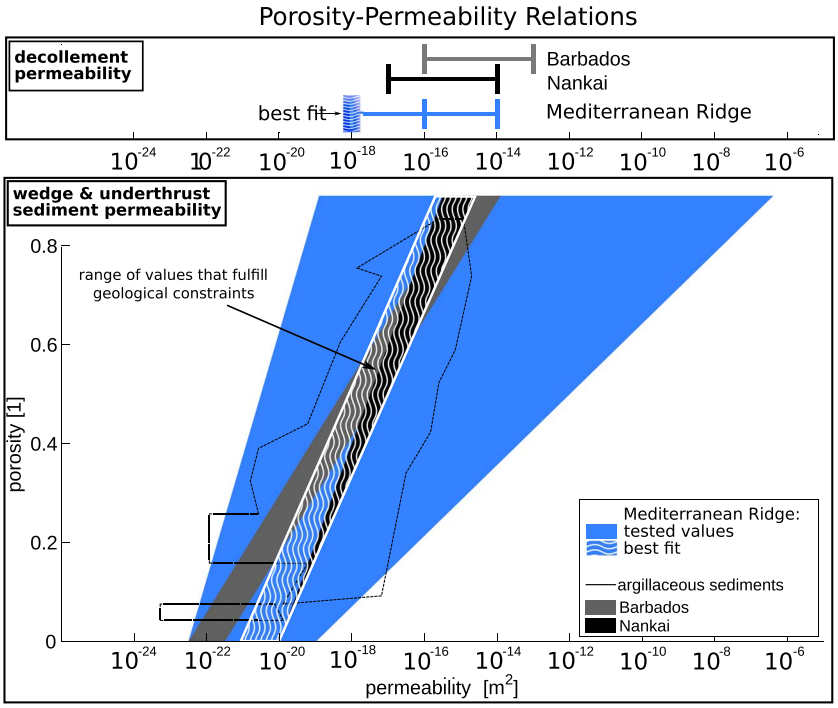

Figure 14. Porosity-permeability relationships and decollement permeabilities tested during the sensitivity analysis together with relationships from other accretionary systems: the relation for argillaceous sediments was derived by *Neuzil* [1994] by comparing laboratory tests and regional studies. The Barbados relation was obtained by numerical modeling by *Bekins et al.* [1995]. Nankai relation is from numerical modeling by *Saffer and Bekins* [1998]. The blue area was tested in this study. The white-shaded area enclose the results accepted by the sensitivity analysis for the MedRidge.

The dehydration source term (Figure 13) is highest deep in the complex because temperature and residence time are highest there. However, the amount of fluid that is produced during the smectite-to-illite reaction is several magnitudes smaller than that originating from compaction in the frontal portion. Although small, the dehydration source term increases continuously toward the backstop and with depth, whereas the compaction-induced dewatering decreases with distance from the deformation front. Peak production from dehydration in the central profile is 7.9^{-21} $\mathrm{Volume_{fluid}/Volume_{bulk}} \cdot \mathrm{s}$ approximately 100 km from the deformation front at a depth of 4.4 km. In the western profile, peak production of 6.18^{-18} $\mathrm{Volume_{fluid}/Volume_{bulk}} \cdot \mathrm{s}$ occurs 170 km away from the deformation front at a depth of 8.9 km.

5.2. Sensitivity Analysis of Permeability

The permeability range applied for the sensitivity study includes possible scenarios from argillaceous sediments [*Neuzil*, 1994] to relationships established by numerical models of other accretionary complexes [*Saffer and Bekins*, 1998; *Bekins et al.*, 1995] (Figure 14). The permeability-porosity relationship dramatically affects flow paths and fluid pressure distribution in the model domain. The following systematic correlations could be deduced: First, the more permeable the decollement is, the smaller is the maximum fluid pressure value in the model domain (provided γ and k_0 are kept constant). If the permeability contrast between the base of the wedge and the decollement exceeds 3 orders of magnitude, all fluid drains along the decollement. Second, higher values of $\log(k_0)$ result in lower pore pressures. Third, the smaller the slope of the porosity-permeability relationship, the higher is the resulting fluid pressure. Considering the fact that no pronounced drainage structures or pore water anomalies were measured at the toe of the MedRidge [*Emeis et al.*, 1996], we exclude results that showed a pronounced flow through the decollement. Furthermore, results with fluid flow occurring downdip were excluded, because such results disagree with intense mud volcanism along the MedRidge indicating that fluids leave the complex. Generally, we did not allow supralithostatic pressure values to evolve because such conditions are short-term phenomena [*Matmon and Bekins*, 2006]. Only in the central profile we allowed supralithostatic fluid pressures in the frontal toe region, because this region suffers deformation due to the collision with the Libyan promontory in addition to the already high strain in the toe region. Therefore, additional fracture zones are likely to evolve and supralitho-

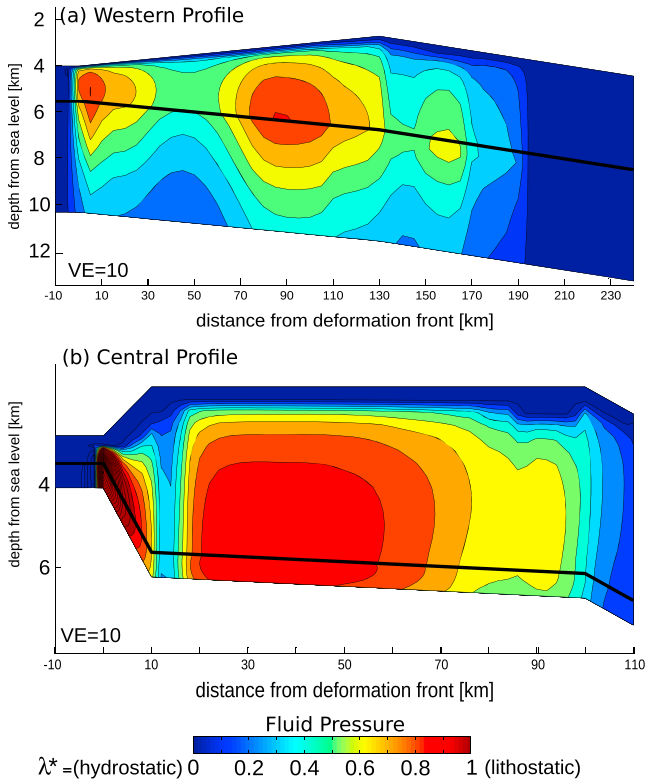

Figure 15. Fluid pressure distribution in terms of the normalized pore pressure ratio $\lambda^{\star}$. (a) Western domain, permeability parameters: $k_d = 10^{-18}$ m^2, $k_0 = 10^{-20}$ m^2, $\gamma = 6$. (b) Central domain, permeability parameters: $k_d = 10^{-18}$ m^2, $k_0 = 10^{-21}$ m^2, $\gamma = 6$. k_0 and γ are parameters in equation (5), k_d is the permeability value of the decollement. Decollement location is indicated as black line in this figure.

static pressure may occur locally and temporarily. From all these constraints, only a relatively narrow range of parameters yields realistic permeability combinations (Figure 14, white area: log(k_0) −20 to −21, $\gamma = 6$; see the best fit permeability distribution along the profiles in Figure 9). Regarding the permeability in the wedge and underthrust succession, the MedRidge porosity-permeability relationship is in a similar range to those established for the Nankai and Barbados accretionary complexes [*Saffer and Bekins*, 1998; *Bekins et al.*, 1995]. Regarding the decollement permeability, models using $k_d = 10^{-18}$ m^2 yield moderate drainage toward the toe of the MedRidge. From this analysis, we can deduce that the higher percentage of evaporite minerals (western profile) and the higher compactional state of sediments in the central profile does compared to other accretionary complexes result in lower sediment porosities in general (see section 4.2) but not in a dramatically different relation between porosity and permeability. However, the lower decollement permeability may be attributed to the extraordinarry lithology and compaction state of the MedRidge. We will further discuss similarities and differences between MedRidge and other subduction systems in section 6.3.

5.3. Fluid Pressure and Flow Velocities

Figure 15 shows the fluid pressure distribution using the permeability parameters that yield the highest acceptable fluid pressure in the model domains. Fluid pressure (P_f) is expressed in terms of the normalized pore pressure ratio $\lambda^{\star} = P_f - P_h / P_l - P_h$, where $\lambda^{\star} = 0$ equals hydrostatic pressure (P_h) and $\lambda^{\star} = 1$ equals lithostatic pressure (P_l). The highest acceptable values for fluid pressure in the western profile (Figure 15a) arise from $\gamma = 6$ and $k_0 = 10^{-20}$ m^2. For this permeability input, the point of maximum fluid pressure is located just above the decollement, and a broad region of high fluid overpressure is confined to the frontal approximately 140 km. Excess fluid pressure decreases toward the backstop. For the central profile, the permeability parameter combination $\gamma = 6$ and $k_0 = 10^{-21}$ m^2 yields the highest fluid pressure values under the constraint that fluid pressure exceeds lithostatic values in the frontal part (Figure 15b). Further, landward from the deformation front, the fluid pressure is constantly high but does not exceed lithostatic values. Fluid pressure finally drops to near hydrostatic values near the backstop. When comparing the western and central profiles, an astonishing similarity in pore pressure magnitude and distribution is overlain by a prominent

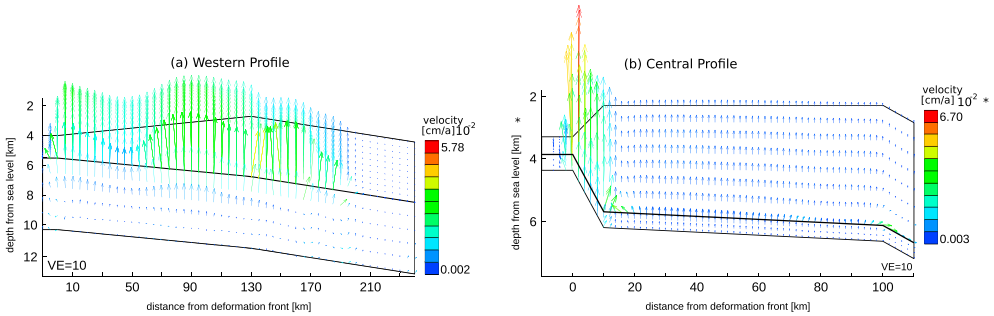

Figure 16. Darcian flow velocities for the western (a) and central (b) profile. The orientation of the arrows indicates the flow direction, the color and length indicates the flow velocity.

compression in the central domain. Here fluid pressure peaks are very closely spaced, most likely reflecting the accentuated shortening in a quasi continent-continent-collision scenario with no downgoing oceanic seafloor remaining.

Using these pressure values, we can further calculate velocities that arise from pressure- and gravity-driven flow. These velocities define the fluid flow field with respect to the sedimentary matrix (Darcian velocities, Figure 16). Darcian velocities are mainly orientated upward to the sea bottom and arise from the pressure distribution plotted in Figure 15. If only the vertical velocity component is considered, the mean value of the Darcian velocity V_y in the wedge of the western profile is 1.54^{-2} cm/a and in the underthrust sediment 0.34^{-2} cm/a. For the central profile, the Darcian velocities are highest (6.74^{-2} cm/a) in the frontal 10 km behind the deformation front and relatively constant but smaller within the rest of the model domain. These Darcian fluid velocities are on average 2 orders of magnitude smaller than the tectonic velocities, which is to be attributed to the low intrinsic permeability in the model domain.

6. Discussion

The discussion serves two main purposes: To underline in what respect the numerical models for the MedRidge are based on a comprehensive data analysis and to illustrate how the geodynamic setting of the MedRidge accretionary complex accentuates deformation and fluid expulsion when compared to other large prisms such as those of Nankai or Barbados. First, the calculated distribution of fluid pressure and flow velocities will be discussed in order to understand the parameters that cause the obtained constellation (section 6.1). Then we assess the resulting consequences for wedge geometry and flow paths within the MedRidge accretionary system (section 6.2). Finally, we compare these results to other subduction systems with large accretionary prisms (section 6.3).

6.1. Fluid Sources and Pressure Distribution

When looking at the toolbox and database of this study, the MedRidge model presented here differs from previous hydrogeological numerical models applied to other accretionary complexes because we do not describe sediment porosity in the model domain by an universal porosity-decay function but by deriving porosity values from seismic interval velocities and interpolating them into the model domain. Despite the obvious advantage of being close to the natural conditions, the resulting compaction source and fluid pressure distribution are partly relatively spiky (e.g., the three domains of elevated pore pressure in the western profile; Figure 15). These localized spikes may be less pronounced in situ, however, seem to best reflect the observational data within the simplified model geometry and grid. Based on the porosity distribution from *P* wave velocities, the location of the peaks in calculated fluid pressure is capable of indicating fluid pressure trends in the MedRidge. This finding further implies that the sensitivity analysis from permeability (see section 5.2 above) yields a minimum estimate for permeability because the cutoff value is governed by the peak fluid pressure value. In other words, when ignoring the peaks in the model results, the overall permeability is low and favors elevated pore fluid pressures (see below). Additionally, the conversion procedure from seismic interval velocities to porosity values heritages errors in absolute values for porosity. However, it is mostly the relative porosity distribution in the model domain that influences the location of the peaks in fluid pressure distribution (see equations (6)–(8)). To evaluate the impact of the uncertainty in porosity

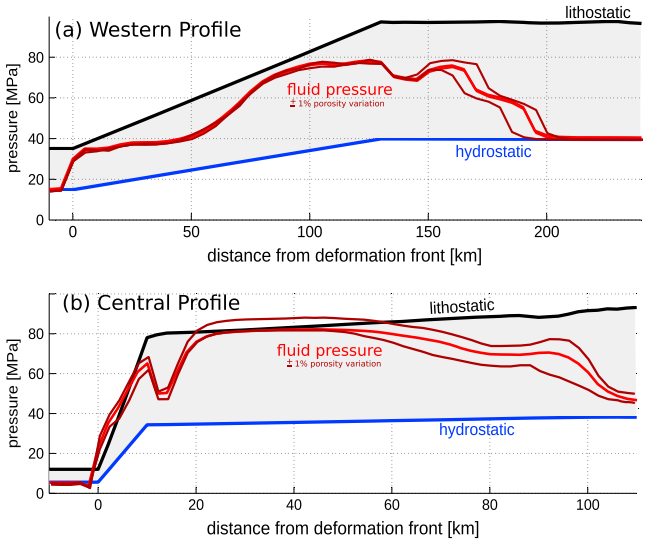

Figure 17. Absolute fluid pressure along the model nodes above the decollement for the pressure distribution plotted in Figure 15 (red line). The black and blue lines give theoretical values for lithostatic and hydrostatic pressure, respectively, calculated at the decollement depth. The dark red lines are the fluid pressure distribution that would arise using porosity values in a range of 2% around the porosities plotted in Figure 8.

distribution, we calculated the fluid pressure additionally using porosities in the range of 2% around the original values (see error range in Figure 17). The general shape of the distribution is consistent, only the distance from the deformation front at which the elevated pressure starts to decrease varies slightly.

Regarding the calculated fluid pressure, the evolution at the decollement level is crucial as it directly mediates the effective stress, and hence the fault strength. In Figure 17 the computed absolute values of fluid pressure for the nodes just above the decollement are plotted. In the frontal part, where the compaction source term is high, the fluid pressure is also high. In the backstop area, where the dehydration source is maximal the fluid pressure tends toward hydrostatic. This observation may be explained by an overall small dehydration source term, which results from the cold thermal regime in the complex. To account for the fact that the modeled temperature distribution (see Figures 10 and 11 above) describes rather an end-member case compared to measurements in the MedRidge, we further tested the sensitivity of the pore pressure to different thermal gradients spanning the whole range of measured values for the western profile (where the temperature variation is larger than in the central domain given the greater depth range). The resulting pore pressure distributions above the decollement are plotted in Figure 18. For gradients smaller than 10°C/km, the influence is insignificant. For a thermal gradient between 15 and 20°C/km, the dehydration source term has a clear impact on the fluid pressure with local supralithostatic values. The effect of the larger dehydration source term is most pronounced between profile kilometers 80 and 130, where the maximum in compaction source term already resulted in a maximum in fluid pressure. When spinning this further, even

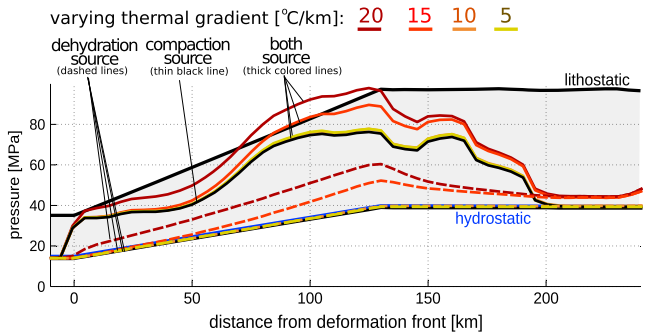

Figure 18. Influence of thermal gradient used to calculate the dehydration source on pore pressure above the decollement for the western profile.

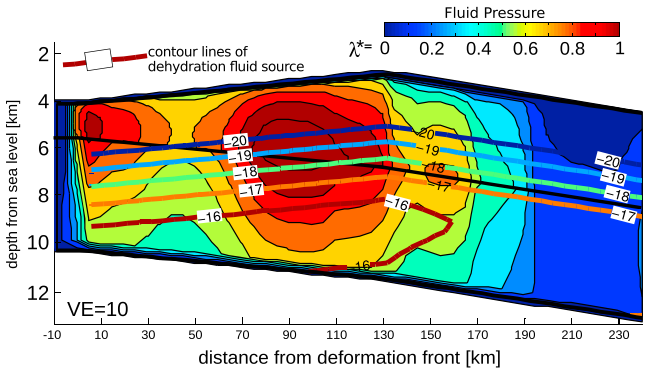

Figure 19. Dehydration source term (contours, in log(Volume$_{fluid}$/Volume$_{bulk}$ · s))) and fluid pressure (color scale; $\lambda^\star$ in [1]) assuming a thermal gradient of 20°C/km. For absolute pressure above the decollement, see dark red line in Figure 18.

in the case of an enhanced thermal gradient and a very thick underthrust sediment section (see pressure distribution in Figure 19), the compaction source remains twice as big as the dehydration source term. We therefore propose that compaction due to thickening of the wedge and lateral compressional stress are the main controlling factors of fluid pressure buildup in the MedRidge. This also demonstrates that compaction disequilibrium remains the most important cause for fluid pressures in case thick, compacting sediments enter the subduction zone and get incorporated into an accretionary prism with very low taper angle.

6.2. Implications on Wedge Geometry, Frictional Behavior, and Fluid Pathways

To evaluate the implications of our hydrogeological results for the MedRidge geometry we undertook a critical taper analysis for the western profile. For the central profile, where the accretionary complex is compressed by the advancing Libyan margin, the assumption of a wedge of a self adjusting wedge is not valid. We followed *Dahlen* [1990] who constrained the critical taper angle of the wedge as a function of pore pressure ratio and coefficient of sliding friction in the wedge and along the decollement. In Figure 20 the surface slope angle is plotted versus the decollement dip, where straight lines in this plot yield a wedge at critical state with constant values of fluid pressure and friction coefficients. Three different cases of fluid pressure configuration are compared: (1) no excess pore pressure is present, (2) the average fluid pressure gained from numerical modeling, and (3) fluid pressure values 10% higher than this maximum value. In all plots, the friction coefficient of the wedge sediments is held constant at the highest value gained by the ring shear experiments ($\mu = 0.62$, Table 2), assuming quartz- and feldspar-rich accreted strata. The basal friction coefficient is assumed to be very low ($\mu_{base} = 0.05$–0.1) based on findings from other accretionary complexes [*Saffer and Tobin*, 2011; *Brown et al.*, 2003].

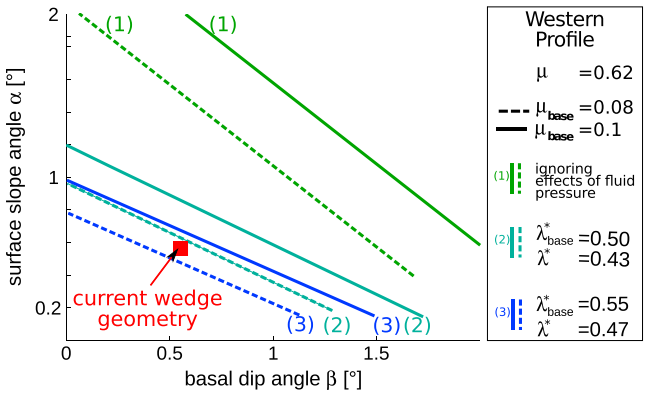

Figure 20. Critical taper analysis for the western profile for different values of (basal) shear coefficient ($\mu_{(base)}$) and fluid pressure in the wedge $\lambda^\star$ and above the decollement $\lambda^\star_{base}$ (pressure values here are given in terms of the modified pore pressure ratio $\lambda^\star = P_f - P_h/P_l - P_h$). A critical Coulomb wedge is maintained along the plotted lines. The red rectangle encloses the area with MedRidge geometry. Line (2) encompasses the averages fluid pressure values from modeling.

From this range of plotted friction and pore pressure configurations, it is obvious that fluid overpressure is important to explain the overall MedRidge geometry. To yield a critical wedge for the western profile using the modeled fluid pressure, the effective basal coefficient of friction must be approximately 0.08 (Figure 20, line (2)). A MedRidge taper angle of 1° with basal friction coefficients consistent with the lower range of determined values from ring shear tests can only be explained when we assume fluid pressures exceeding 10% of the maximal model result (Figure 20, line 3). Different scenarios are likely to explain this discrepancy or justify such an assumption: First, as had been discussed in section 6.1 the modeled permeabilities describe a threshold estimate, because the sensitivity analysis was governed by the peak fluid pressure rather than its average value. Consequently, lower permeabilities in the wedge sediments would favor higher pore pressure at the decollement. Second, Figure 18 attests that a higher-temperature gradient could provide a higher dehydration source term.

The critical taper analysis demonstrates that elevated fluid pressures at the decollement level and a low-permeable wedge are mandatory to explain the low taper angle of the western MedRidge. However, to explain the transport of fluid with an anomalous pore water geochemistry from depth to the seafloor, as it was observed at mud volcanoes in the MedRidge [*Deyhle and Kopf*, 2001], transient flow along highly permeable fault zones must occur. Episodic flow along such fault zones would allow pore pressure at the decollement to remain high as required by the critical taper analysis for most of the time but could explain the temporally varying activity of mud volcanoes and drops in pore pressure at other times.

Using the modeled fluid pressure values and the range of friction coefficients derived from the ring shear tests (see section 3.2.2 above), the shear stress along the decollement can be constrained. With friction coefficients between 0.16 and 0.45, the shear stress in the western profile ranges from 0.1 MPa to 0.25 MPa at a distance of 100 km from the deformation front and reaches 6 MPa to 26 MPa at the backstop. In the central profile shear stress is smaller than 1 MPa at 50 km from the deformation front and between 4 MPa and 22 MPa at the backstop for the same friction coefficients. These low shear stresses along the decollement indicate a weak fault. Such weak basal strata in wedges favor small taper angles. However, the mechanical weakness also favors aseismic behavior and suppresses runaway slip behavior [*Saffer and Tobin*, 2011]. Therefore, it could provide a possible explanation for the absence of large earthquakes in the frontal part of the subduction system over the last centuries despite the incipient collision in the mature Hellenic subduction system [*Ambraseys and Jackson*, 1998; *Shaw and Jackson*, 2010]. The reduction of fluid overpressure underneath the backstop and the associated increase in shear stress may facilitate unstable sliding of the sediment and could mark the onset of the updip limit of the seismogenic zone (*Scholz* [1998]; *Meier et al.* [2004]).

6.3. Comparison Between the MedRidge and the Nankai and Barbados Accretionary Complexes

Unlike the Nankai Trough or Barbados regions, the MedRidge shows a very pronounced along-strike variation, most notably as a result of a continuously changing setting from orthogonal to oblique subduction as well as the indentation of the Libyan promontory south of Crete. As a direct consequence, the western MedRidge has a relatively thick underthrust sediment sequence, and the modeled temperature regime is rather cold (see Figures 4 and 10 above). In the central portion, however, most oceanic crust is consumed and sediment thickness as well as heat flow are similar to Nankai and Barbados (see Table 1 and section 6.2 above). The main difference in calculated fluid pressure values between the western MedRidge and Barbados or Nankai is that in the former case high fluid pressure is conserved at large distance from the deformation front. To evaluate to which extent this high fluid pressure in the western profile is influenced by thickness of underthrust sediments and/or temperature, we run models, varying these parameters (Figure 21) and further consult the central profile along which the incoming sediment equals that of Barbados and Nankai in broad terms. In the case of a cold temperature regime (Figure 21a) the fluid pressures are smaller than in the case of a warm regime (Figure 21b). For a thinner underthrust section, the pore pressure distribution shows smaller magnitudes and fewer spikes, but the high fluid pressure values are nevertheless conserved to great distances from the deformation front. This implies that (1) the fluid pressures in the MedRidge at large distances from the deformation front result mainly from the used porosity distribution which yields a high fluid source term there and (2) the thickness of underthrust sediments plays an important key role in the magnitude of those fluid pressures.

Nevertheless, given that the high fluid pressure is still visible in models using a higher temperature gradient and a thinner underthrust sediment section (Figures 18, 19, and 21). Therefore, it is a very likely scenario that

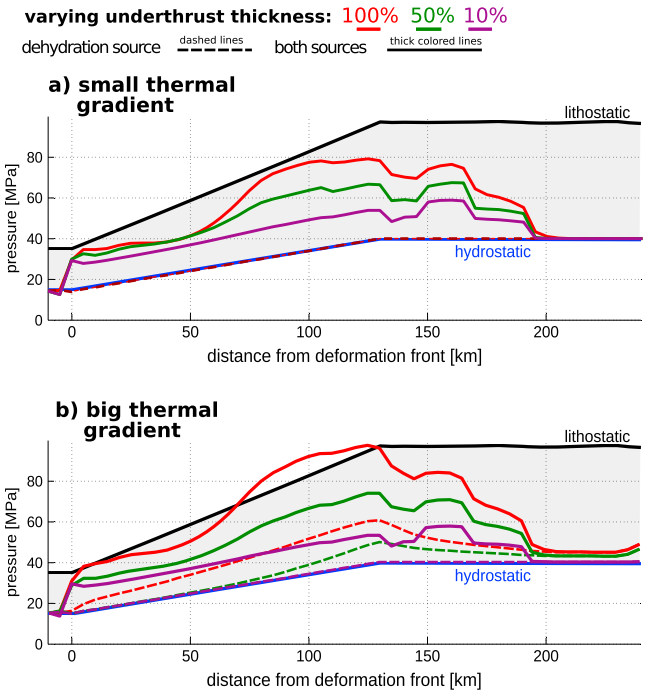

Figure 21. Influence of changing thickness of underthrust sediments on fluid pressure above the decollement in the western profile for a thermal gradient of (a) 5°C/km and (b) 20°C/km. The thickness of the underthrust sediments is 50% and 10% of the original thickness given in Table 3. The new model parameters are calculated assuming that the depth extend of the underthrust sequence is smaller by 50% and 90%, respectively.

certain amounts of salt had been entering the subduction system during the Messinian salinity crisis [*Reston et al.*, 2002]. These low-permeability deposits may facilitate the formation of a hydraulic barrier, preventing the compaction and pore fluid escape near the deformation front and in or underneath the frontal prism. In the pre-Messinian portion of the MedRidge and underthrust sequence (i.e., 90 km behind the deformation front), this barrier does not exist, allowing fluids to escape to the seafloor. This scenario would further be supported by the anomalous high rate of mud volcanism near the backstop (i.e., >150 inward of the deformation front). Considering the fact that at such a distance from the toe, the decollement permeability is too low to effectively channelize flow toward the trench in our MedRidge model, the bulk of the fluid volume produced in the underthrust sediments is likely to migrate upward rather than along the decollement. There, permeability is still low, because the sediments are highly compacted, causing a peak in pore pressure. However, evidence from recent expeditions exists that under consolidated mud of epizone diagenetic signature also carries deep-seated fluids from depth to the seafloor, both along back thrust faults and mud volcanoes [*Kopf et al.*, 2012]. Temporarily active mud volcanism [e.g., *Emeis et al.*, 1996] could then act as a valve for the fluids to escape to the sea bottom in large volumes, as attested by calculations [*Kopf et al.*, 2001]. Such mud volcanoes carrying fluids of deep-seated origin occur in similar locations in the Nankai Trough, most prominently in the Kumano Basin [*Toki et al.*, 2004; *Kopf and Shipboard Party*, 2013]. Similarly, mud volcanoes are found in various places in the Barbados subduction system [*Brown and Westbrook*, 1988], even on the island of Barbados itself. In summary, this indicates that a large number of similarities exist between those regions.

When now regarding the central profile the thickness of the incoming sediment is also similar to Nankai and Barbados. Furthermore, the central MedRidge section was above sea level during the Messinian desiccation, so that evaporites do not exist here—again, in agreement with Nankai and Barbados. We can hence use the central profile to study the effects of the advanced compression due to the advancing Libyan Margin, or—more generally speaking—a mature collisional setting and its effects on hydrogeological drivers. From the modeling results of this study, the enhanced collision could foster efficient compaction of the prism and incoming sediments, hence prevent fluids to rise rapidly and explain the elevated pore pressure at the MedRidge decollement (Figure 17) as well as the steep taper angle (see above). We can further develop a

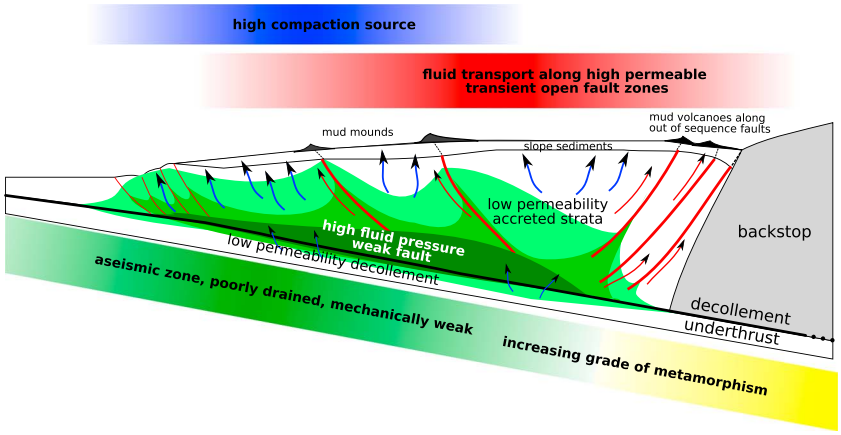

Figure 22. Schematic cross section through the accretionary system illustrating the implications of the model results for the hydrogeological environment of the MedRidge. Arrows represent fluid flow directions relative to the sediment matrix. Blue arrows represent flow through bulk matrix, and red arrows represent flow along highly permeable faults. The green-shaded area encloses areas of high fluid pressure.

conceptual model for the Mediterranean Ridge accretionary complex (Figure 22), which also applies to other systems with wide accretionary complexes without the need for significant modifications.

7. Conclusions

1. We assessed the hydrogeology of the Mediterranean Ridge using a numerical approach based on the conservation of fluid mass and the validity of Darcy's law. Two profiles were set up that reflect the along-strike variation in wedge geometry. A sensitivity analysis, which was undertaken to establish a permeability (k)-porosity (n) relationship for the model domains, yielded low permeability values for both profiles, which is consistent with findings at other accretionary complexes [*Saffer and Tobin*, 2011].
2. A relatively impermeable decollement ($k_d = 10^{-18}$ m^2) likely hampers drainage toward the toe and causes elevated pore pressures along it. In our model, the peak compactional fluid source by far dominates the dehydration source even if a relatively warm thermal gradient (20°C/km) or a thin (~1 km) underthrust sequence is assumed in the model domain.
3. The comparison to other accretionary margins such as Nankai or Barbados is feasible, and the similar characteristics regarding fluid pressure are schematically summarized in a conceptual model (Figure 22). This includes zones of (temporarily) high permeability to feed-active, deep-seated mud volcanoes landward of the deformation front. However, in the Mediterranean the presence of evaporites, the thick underthrust sequence, and/or the advanced collision between Africa and Eurasia accentuate deformation and likely help maintain high fluid pressures, in places in excess of lithostatic.
4. Critical taper modeling attested that a combination of very low basal friction coefficients and enhanced fluid pressures can explain the observed wedge geometry along the MedRidge profiles studied. This implies that mud volcanoes, which act as fluid valves all the way to the backstop, can only be temporally active to maintain the overall high pore pressure values at the decollement level.

Acknowledgments
The geotechnical part of this study is based on samples gained during the research cruise P410 MUDFLOW and ODP (Ocean Drilling Program) Leg 160. We thank the crews as well as the scientific parties of these cruises. Samples were provided by the Ocean Drilling Program. ODP was sponsored by the U.S. National Science Foundation (NSF) and participating countries under management of Joint Oceanographic Institutions (JOI). Christoph Vogt is thanked for XRD analyses and Dirk Kläschen for kindly providing the seismic data. This paper benefited from the discussion and comments by Friedemann Wenzel as well as Gauvain Wiemer and Matt Ikari. Funding for this research was provided by the German Science Foundation (DFG) to A. Kopf and to A. Hüpers (grants KO2108/11-1 and HU1789/2-1).

References

Ambraseys, N., and J. Jackson (1998), Faulting associated with historical and recent earthquakes in the eastern Mediterranean region, *Geophys. J. Int.*, *133*(2), 390–406, doi:10.1046/j.1365-246X.1998.00508.x.

Athy, L. (1930), Density, porosity, and compaction of sedimentary rocks, *Am. Assoc. Pet. Geol. Bull.*, *14*(1), 1–24.

Bekins, B., and S. Dreiss (1992), A simplified analysis of parameters controlling dewatering in accretionary prisms, *Earth Planet. Sci. Lett.*, *109*(3-4), 275–287, doi:10.1016/0012-821X(92)90092-A.

Bekins, B., A. McCaffrey, and S. Dreiss (1995), Episodic and constant flow models for the origin of low-chloride waters in a modern accretionary complex, *Water Resour. Res.*, *31*(12), 3205–3215, doi:10.1029/95WR02569.

Biju-Duval, B., P. Le Quellec, A. Mascle, V. Renard, and P. Valery (1982), Multibeam bathymetric survey and high resolution seismic investigations on the Barbados Ridge Complex (eastern Caribbean): A key to the knowledge and interpretation of an accretionary wedge, *Tectonophysics*, *86*(1), 275–304.

Bray, C., and D. Karig (1985), Porosity of sediments in accretionary prisms and some implications for dewatering processes, *J. Geophys. Res.*, *90*(B1), 768–778, doi:10.1029/JB090iB01p00768.

Brown, K., and G. Westbrook (1988), Mud diapirism and subcretion in the Barbados Ridge accretionary complex: The role of fluids in accretionary processes, *Tectonics*, *7*(3), 613–640.

Brown, K., A. Kopf, M. Underwood, and J. Weinberger (2003), Compositional and fluid pressure controls on the state of stress on the Nankai Subduction Thrust: A weak plate boundary, *Earth Planet. Sci. Lett.*, *214*(3-4), 589–603, doi:10.1016/S0012-821X(03)00388-1.

Camerlenghi, A., M. Cita, B. Vedova, N. Fusi, L. Mirabile, and G. Pellis (1995), Geophysical evidence of mud diapirism on the Mediterranean Ridge Accretionary Complex, *Mar. Geophys. Res.*, *17*(2), 115–141, doi:10.1007/BF01203423.

Chaumillon, E., and J. Mascle (1997), From foreland to forearc domains: New multichannel seismic reflection survey of the Mediterranean Ridge Accretionary Complex (eastern Mediterranean), *Mar. Geol.*, *138*(3), 237–259, doi:10.1016/S0025-3227(97)00002-9.

Chaumillon, E., J. Mascle, and H. Hoffmann (1996), Deformation of the western Mediterranean Ridge: Importance of Messinian evaporitic formations, *Tectonophysics*, *263*(1-4), 163–190, doi:10.1016/S0040-1951(96)00035-2.

Clift, P., and P. Vannucchi (2004), Controls on tectonic accretion versus erosion in subduction zones: Implications for the origin and recycling of the continental crust, *Rev. Geophys.*, *42*, RG2001, doi:10.1029/2003RG000127.

Cochrane, G., J. Moore, M. MacKay, and G. Moore (1994), Velocity and inferred porosity model of the Oregon Accretionary Prism from multichannel seismic reflection data: Implications on sediment dewatering and overpressure, *J. Geophys. Res.*, *99*(B4), 7033–7043, doi:10.1029/93JB03206.

Costa Pisani, P., M. Reshef, and G. Moore (2005), Targeted 3-D prestack depth imaging at Legs 190–196 ODP drill sites (Nankai Trough, Japan), *Geophys. Res. Lett.*, *32*, L20309, doi:10.1029/2005GL024191.

Dahlen, F. (1990), Critical taper model of fold-and-thrust belts and accretionary wedges, *Annu. Rev. Earth Planet. Sci.*, *18*, 55–99.

Davis, D., J. Suppe, and F. Dahlen (1983), Mechanics of fold-and-thrust belts and accretionary wedges, *J. Geophys. Res.*, *88*(B2), 1153–1172, doi:10.1029/JB088iB02p01153.

Dewey, J., W. Pitman, W. Ryan, and J. Bonnin (1973), Plate tectonics and the evolution of the Alpine system, *Geol. Soc. Am. Bull.*, *84*(10), 3137–3180, doi:10.1130/0016-7606(1973)84<3137:PTATEO>2.0.CO;2.

Deyhle, A., and A. Kopf (2001), Deep fluids and ancient pore waters at the backstop: Stable isotope systematics (B, C, O) of mud-volcano deposits on the Mediterranean Ridge Accretionary Wedge, *Geology*, *29* (11), 1031–1034, doi:10.1130/0091-7613(2001)029<1031:DFAAPW>2.0.CO;2.

Emeis, K.-C., et al. (1996), *Proceedings of the Ocean Drilling Program Initial Reports Leg, 160*, Ocean Drilling Program, College Station, TX.

Erickson, S., and R. Jarrard (1998), Velocity-porosity relationships for water-saturated siliciclastic sediments, *J. Geophys. Res.*, *103*(B12), 30,385–30,406, doi:10.1029/98JB02128.

Ferguson, I., G. Westbrook, M. Langseth, and G. Thomas (1993), Heat flow and thermal models of the Barbados Ridge Accretionary Complex, *J. Geophys. Res.*, *98*(B3), 4121–4142, doi:10.1029/92JB01853.

Hamamoto, H., M. Yamano, S. Goto, M. Kinoshita, K. Fujino, and K. Wang (2011), Heat flow distribution and thermal structure of the Nankai subduction zone off the Kii Peninsula, *Geochem. Geophys. Geosyst.*, *12*, Q0AD20, doi:10.1029/2011GC003623.

Henry, P., and C.-Y. Wang (1991), Modeling of fluid flow and pore pressure at the toe of Oregon and Barbados Accretionary Wedges, *J. Geophys. Res.*, *96*(B12), 20,109–20,130.

Hoffman, N., and H. Tobin (2004), An empirical relationship between velocity and porosity for underthrust sediments of the Nankai Trough Accretionary Prism, in *Proceedings of the Ocean Drilling Program, Scientific Results*, vol. 190–196, edited by H. Mikada et al.

Huguen, C., N. Chamot-Rooke, B. Loubrieu, and J. Mascle (2006), Morphology of a pre-collisional, salt-bearing, accretionary complex: The Mediterranean Ridge (eastern Mediterranean), *Mar. Geophys. Res.*, *27*(1), 61–75, doi:10.1007/s11001-005-5026-5.

Hyndman, R., G. Moore, and K. Moran (1993), Velocity, porosity and pore-fluid loss from the Nankai subduction zone accretionary prism, *Proc. Ocean Drill. Program, Sci. Results*, *131*, 211–220.

Karig, D., and C. Angevine (1986), Geologic constraints on subduction rates in the Nankai Trough, in *Initial Reports of the Deep Sea Drilling Project*, vol. 87, edited by D. E. Karig et al., pp. 789–796, U.S. Government Printing Office, Washington, D. C.

Kastens, K. (1991), Rate of outward growth of the Mediterranean Ridge Accretionary Complex, *Tectonophysics*, *199*(1), 25–50, doi:10.1016/0040-1951(91)90117-B.

Kastens, K., N. Breen, and M. Cita (1992), Progressive deformation of an evaporite-bearing accretionary complex: SeaMARC I, SeaBeam and piston-core observations from the Mediterranean Ridge, *Mar. Geophys. Res.*, *14*, 249–298, doi:10.1007/BF01203620.

Kobayashi, K., S. Kasuga, and K. Okino (1995), Shikoku Basin and its margins, in *Backarc Basins: Tectonics and Magmatism*, edited by B. Taylor pp. 381–405, Plenum Press, New York.

Kopf, A., and Shipboard Party (2013), *Report and Preliminary Results of RV Sonne Cruise SO222 MEMO (MeBo drilling and in situ Long-Term monitoring in the Nankai Trough Accretionary Complex, Japan), 297*, Bremen, Berichte aus dem Fachbereich Geowissenschaften der Universität Bremen.

Kopf, A., D. Klaeschen, and J. Mascle (2001), Extreme efficiency of mud volcanism in dewatering accretionary prisms, *Earth Planet. Sci. Lett.*, *189*(3-4), 295–313, doi:10.1016/S0012-821X(01)00278-3.

Kopf, A., J. Mascle, and D. Klaeschen (2003), The Mediterranean Ridge: A mass balance across the fastest growing accretionary complex on Earth, *J. Geophys. Res.*, *108*(B8), 2372, doi:10.1029/2001JB000473.

Kopf, A., et al. (2012), *Report and Preliminary Results of RV POSEIDON Cruise P410. MUDFLOW (Mud Volcanism, Faulting and Fluid Flow on the Mediterranean Ridge Accretionary Complex), 284*, Bremen, Berichte aus dem Fachbereich Geowissenschaften der Universität Bremen.

Le Pichon, X., N. Chamot-Rooke, S. Lallemant, R. Noomen, and G. Veis (1995), Geodetic determination of the kinematics of central Greece with respect to Europe: Implications for eastern Mediterranean tectonics, *J. Geophys. Res.*, *100*(B7), 12,675–12,690, doi:10.1029/95JB00317.

Logan, J. M. (1978), Creep, stable sliding, and premonitory slip, *Pure Appl. Geophys.*, *116*(4-5), 773–789, doi:10.1007/BF00876538.

Mascle, A., B. Biju-Duval, P. De Clarens, and H. Munsch (1986), Growth of accretionary prisms: Tectonic processes from Caribbean examples, in *The Origin of Arcs, Develpoment in Geotecttonics*, vol. 21, edited by F. C. Wezel pp. 375–400, Elsevier, Amsterdam, Netherlands.

Matmon, D., and B. Bekins (2006), Hydromechanics of a high taper angle, low-permeability prism: A case study from Peru, *J. Geophys. Res.*, *111*(B7), B07101, doi:10.1029/2005JB003697.

Meier, T., M. Rische, B. Endrun, A. Vafidis, and H.-P. Harjes (2004), Seismicity of the Hellenic subduction zone in the area of western and central Crete observed by temporary local seismic networks, *Tectonophysics*, *383*(3), 149–169.

Minning, M., D. Hebbeln, C. Hensen, and A. Kopf (2006), Geotechnical and geochemical investigations of the Marquês de Pombal landslide at the Portuguese continental margin, *Nor. Geol. Tidsskr.*, *86*(3), 187.

Moore, G. F., et al. (2001), New insights into deformation and fluid flow processes in the Nankai Trough Accretionary Prism: Results of Ocean Drilling Program Leg 190, *Geochem. Geophys. Geosyst.*, *2*(10), 1058, doi:10.1029/2001GC000166.

Moore, J., C. Rowe, and F. Meneghini (2007), How accretionary prisms elucidate seismogenesis in subduction zones, in *The Seismogenic Zone of Subduction Thrust Faults*, edited by T. H. Dixon and J. C. Moore, pp. 288, New York.

Moore, J. C., and D. Saffer (2001), Updip limit of the seismogenic zone beneath the accretionary prism of southwest Japan: An effect of diagenetic to low-grade metamorphic processes and increasing effective stress, *Geology*, *9*(2), 183–186, doi:10.1130/0091-7613(2001)029<0183:ULOTSZ>2.0.CO;2.

Moore, J. C., et al. (1988), Tectonics and hydrogeology of the northern Barbados Ridge: Results from Ocean Drilling Program Leg 110, *Geol. Soc. Am. Bull.*, *100*(10), 1578–1593.

Müller, C., and R. Wright (1977), History of the Mediterranean salinity crisis, *Structural history of the Mediterranean basins*, 421.

Müller, R., M. Sdrolias, C. Gaina, and W. Roest (2008), Age, spreading rates, and spreading asymmetry of the world's ocean crust, *Geochem. Geophys. Geosyst.*, *9*, Q04006, doi:10.1029/2007GC001743.

Neuzil, C. (1994), How permeable are clays and shales?, *Water Resour. Res.*, *30*(2), 145–150, doi:10.1029/93WR02930.

Pichon, X., and J. Angelier (1979), The Hellenic arc and trench system: A key to the neotectonic evolution of the eastern Mediterranean area, *Tectonophysics*, *60*(1-2), 1–42, doi:10.1016/0040-1951(79)90131-8.

Pytte, A., and R. Reynolds (1988), The thermal transformation of smectite to illite, in *Thermal History of Sedimentary Basins,* edited by N. D. Naeser and T. H. McCulloh, pp. 133–140, Springer-Verlag, Berlin, doi:10.1007/978-1-4612-3492-0_8.

Rabaute, A., and N. Chamot-Rooke (2007), Quantitative mapping of active mud volcanism at the western Mediterranean Ridge-backstop contact, *Mar. Geophys. Res.*, *28*(3), 271–295, doi:10.1007/s11001-007-9031-8.

Reston, T., R. von Huene, T. Dickmann, D. Klaeschen, and H. Kopp (2002), Frontal accretion along the western Mediterranean Ridge: The effect of Messinian evaporites on wedge mechanics and structural style, *Mar. Geol.*, *186*(1), 59–82, doi:10.1016/S0025-3227(02)00173-1.

Ryan, W., K. J. Hsü, M. B. Cita, P. Dumitrica, J. M. Lort, W. Mayne, W. D. Nesteroff, G. Pautot, H. Stradner, and F. C. Wezel (1973), *Initial Reports of the Deep Sea Drilling Project*, Vol. 13, Washington (U.S. Government Printing Office), doi:10.2973/dsdp.proc.13.101.1973.

Saffer, D., and B. Bekins (1998), Episodic fluid flow in the Nankai Accretionary Complex: Timescale, geochemistry, flow rates, and fluid budget, *J. Geophys. Res.*, *30*(B12), 351–30, doi:10.1029/98JB01983.

Saffer, D., and H. Tobin (2011), Hydrogeology and mechanics of subduction zone forearcs: Fluid flow and pore pressure, *Annu. Rev. Earth Planet. Sci.*, *39*, 157–186, doi:10.1146/annurev-earth-040610-133408.

Saffer, D., M. Underwood, and A. McKiernan (2008), Evaluation of factors controlling smectite transformation and fluid production in subduction zones: Application to the Nankai Trough, *Isl. Arc*, *17*(2), 208–230, doi:10.1111/j.1440-1738.2008.00614.x.

Saffer, D. M., and B. A. Bekins (2006), An evaluation of factors influencing pore pressure in accretionary complexes: Implications for taper angle and wedge mechanics, *J. Geophys. Res.*, *111*(B4), B04101, doi:10.1029/2005JB003990.

Scholz, C. (1998), Earthquakes and friction laws, *Nature*, *391*(6662), 37–42, doi:10.1038/34097.

Sclater, J., C. Jaupart, and D. Galson (1980), The heat flow through oceanic and continental crust and the heat loss of the Earth, *Rev. Geophys.*, *18*(1), 269–311, doi:10.1029/RG018i001p00269.

Screaton, E. J., D. R. Wuthrich, and S. J. Dreiss (1990), Permeabilities, fluid pressures, and flow rates in the Barbados Ridge Complex, *J. Geophys. Res.*, *95*(B6), 8997–9007.

Seno, T. (1977), The instantaneous rotation vector of the Philippine Sea Plate relative to the Eurasian Plate, *Tectonophysics*, *42*(2), 209–226.

Shaw, B., and J. Jackson (2010), Earthquake mechanisms and active tectonics of the Hellenic subduction zone, *Geophys. J. Int.*, *181*(2), 966–984, doi:10.1111/j.1365-246X.2010.04551.x.

Shi, Y., C.-Y. Wang, W.-T. Hwang, and R. von Huene (1989), Hydrogeological modeling of porous flow in the Oregon accretionary prism, *Geology*, *17*(4), 320–323.

Stein, S., C. DeMets, R. G. Gordon, J. Brodholt, D. Argus, J. F. Engeln, P. Lundgren, C. Stein, D. A. Wiens, and D. F. Woods (1988), A test of alternative Caribbean Plate relative motion models, *J. Geophys. Res.*, *93*(B4), 3041–3050.

Steurer, J., and M. Underwood (2003), Clay mineralogy of mudstones from the Nankai Trough reference Sites 1173 and 1177 and frontal accretionary prism Site 1174, *Proc. Ocean Drill. Program Part B Sci. Results.*, *190*, 1–37.

Sun, H., R. Feistel, M. Koch, and A. Markoe (2008), New equations for density, entropy, heat capacity, and potential temperature of a saline thermal fluid, *Deep Sea Res. Part I*, *55*(10), 1304–1310, doi:10.1016/j.dsr.2008.05.011.

Taira, A., et al. (1992), Sediment deformation and hydrogeology of the Nankai Trough accretionary prism: Synthesis of shipboard results of ODP Leg 131, *Earth Planet. Sci. Lett.*, *109*(3), 431–450.

Thomson, S., B. Stöckhert, and M. Brix (1998), Thermochronology of the high-pressure metamorphic rocks of Crete, Greece: Implications for the speed of tectonic processes, *Geology*, *259*(3), doi:10.1130/0091-7613(1998)026<0259:TOTHPM>2.3.CO;2.

Toki, T., U. Tsunogai, T. Gamo, S. Kuramoto, and J. Ashi (2004), Detection of low-chloride fluids beneath a cold seep field on the Nankai Accretionary Wedge off Kumano, south of Japan, *Earth Planet. Sci. Lett.*, *228*(1), 37–47.

Urmos, J., R. Wilkens, F. Bassinot, M Lyle, J. Marsters, L. Mayer, and D. Mosher (1993), Laboratory and well-log velocity and density measurements from the Ontong Java Plateau: New in-situ corrections to laboratory data from pelagic carbonates, *Proc. Ocean Drill. Program Part B Sci. Results.*, *130*, 607.

Vogt, C., J. Lauterjung, and R. Fischer (2002), Investigation of the clay fraction (<2 μm) of the clay mineral society reference clays, *Clays Clay Miner.*, *50*(3), 388.

Voss, C., and A. Provost (1984), *SUTRA. US Geological Survey Water Resources Investigation Reports*, pp. 84–4369.